INTERNATIONAL JOURNAL FOR NUMERICAL METHODS IN FLUIDS, VOL. 15, 453–489 (1992)

# LARGE-EDDY SIMULATION OF TURBULENT FLOW AND HEAT TRANSFER IN PLANE AND RIB-ROUGHENED CHANNELS

M. CIOFALO

*Dipartimento di Ingegneria Nucleare, Universita' di Palermo, Viale delle Scienze, 90128 Palermo, Italy*

AND

M. W. COLLINS

*Thermo-Fluids Engineering Research Centre, City University, Northampton Square, London EC1V 0HB, U.K.*

## SUMMARY

Large-eddy simulation results are presented and discussed for turbulent flow and heat transfer in a plane channel with and without transverse square ribs on one of the walls. They were obtained with the finite-difference code Harwell-FLOW3D, Release 2, by using the PISOC pressure–velocity coupling algorithm, central differencing in space, and Crank–Nicolson time stepping. A simple Smagorinsky model, with van Driest damping near the walls, was implemented to model subgrid scale effects. Periodic boundary conditions were imposed in the streamwise and spanwise directions. The Reynolds number based on hydraulic diameter (twice the channel height) ranged from 10 000 to 40 000. Results are compared with experimental data, $k$–$\varepsilon$ predictions, and previous large-eddy simulations.

KEY WORDS Large-eddy simulation Recirculating flows Rib roughness

## 1. INTRODUCTION

Heat transfer and pressure drop performances are essential data in the design of heat exchangers and other engineering components with substantial economic connotations. However, the physical equations which describe the fluid flow and convective heat transfer are complex partial differential equations (e.g. Navier–Stokes) and require the use of large digital computers. Despite their availability, simplifying assumptions are used whenever possible to reduce computing expenses. In this connection, we may distinguish three different classes of flow solutions, namely, laminar, time-averaged turbulent and direct simulations.

For laminar flows, time-independence and geometrical symmetry are theoretically justifiable, and applications of computer programs, in general, agree very well with experiments. For turbulent flows, Reynolds-averaging of the equations on the basis of time gives laminar-like equations for which also time-independence and symmetry are invoked. In addition, though, a turbulence model is needed to give a turbulent viscosity or turbulent stresses.

However, in fact, both laminar and turbulent flows are described by the same equations, and Spalding, for instance, has pointed out their essential identity.[1] Of much more importance is the fact that turbulence is always four-dimensional (three spatial, one time, co-ordinate) in character.

0271–2091/92/160453–37$23.50

*Received January 1990*
*Revised February 1992*

This is reflected in the fact that it is very difficult to get consistently high-quality predictions using the time-averaged equations, no matter how complex the turbulence model is made.

This turns our attention to direct simulation (DS) of the basic equations, which can therefore treat laminar or turbulent flows of any transient or geometrical character. The only, but very important, reservation to this is that higher turbulence covers such a range of scales that not all parts may be resolved. This alternative is called large-eddy simulation (LES) which requires a subgrid (SG) model for the unresolved scales.[2] This technique has been applied with some success to a number of basic geometries, including homogeneous turbulence, flow in plane channels and annuli, and Bènard convection. However, this has generally been done with specially written computer codes and with the use of numerical methods which are difficult to extend to complex geometries of engineering interest.

On the other hand, computer codes have been developed in the last years which can handle complex geometries, allowing steady or transient simulations of recirculating flows. Some of them make use of finite difference methods in conjunction with body-fitted co-ordinates, making them powerful tools for the study of problems of direct engineering interest. The package Harwell-FLOW3D, Release 2[3] is an example of these codes.

The main purpose of the present study was to demonstrate the feasibility of making a large-eddy simulation of both simple and complex flows with the standard numerics of a general-purpose code. Further, it was intended that the storage and CPU-time requirements would be moderate enough to make the application of LES to engineering problems an attractive possibility, if not an immediately viable actuality. Thus, it was preferred to implement as simple a subgrid model as possible, with primary emphasis on stability and generality rather than on accuracy.

## 2. MODEL AND METHODS

Reviews of the LES method are given e.g. by Voke and Collins,[2] Ferziger,[4] and Grötzbach.[5] Here, we concentrate on the model and methods used for the present simulations in plane and rib-roughened channels.

### *2.1. Equations and subgrid model*

The continuity, momentum (Navier–Stokes) and energy equations for incompressible fluid flow with heat transfer to be solved in LES can be written as follows (see References 6 and 7 for details):

$$\frac{\partial u_i}{\partial x_i}=0, \tag{1}$$

$$\frac{\partial u_i}{\partial t}+\frac{\partial u_i u_j}{\partial x_j}=-\frac{1}{\rho}\frac{\partial P}{\partial x_i}+\frac{\partial}{\partial x_i}\left[(\nu+\nu_s)\left(\frac{\partial u_i}{\partial x_j}+\frac{\partial u_j}{\partial x_i}\right)\right], \tag{2}$$

$$\frac{\partial T}{\partial t}+\frac{\partial u_j T}{\partial x_j}=\frac{\partial}{\partial x_j}\left[(\alpha+\alpha_s)\frac{\partial T}{\partial x_j}\right]. \tag{3}$$

In equations (1)–(3) $u_i$, $P$ and $T$ are *resolved* (i.e. large-scale) fields; a gradient-diffusion (Boussinesq-like) hypothesis on subgrid stresses and heat fluxes is implied; and implicit summation over repeated indices is understood. The specific heat was assumed to be a constant in equation (3). $P$ is *not* the static pressure, $p$; rather, it is defined as

$$P=p+(2/3)\rho\tilde{k}, \tag{4}$$

$\tilde{k}$ being the subgrid (unresolved) turbulent kinetic energy. Note that $P=p$ on walls.

The Smagorinsky model[8] was used here for the subgrid kinematic viscosity $\nu_s$:

$$\nu_s = (c_s D\Delta)^2 (2S_{ij}S_{ij})^{1/2} \tag{5}$$

In this equation, $c_s$ is a model constant of the order of 0·1, $\Delta$ is the average size of the generic computational cell (cubic root of its volume), $D$ is a near-wall damping function expressed following van Driest:[9]

$$D = 1 - \exp[-(y^+/A^+)], \tag{6}$$

where $A^+$ is a constant ($=25$) and $y^+$ is the distance from the nearest wall, expressed in wall units (see Section 2.2 for a discussion of scaling factors to be chosen).

The choice of a value for the Smagorinsky constant, $c_s$, is a crucial issue in LES. Although a value of 0·2–0·3 can be derived from theoretical considerations,[5] in practical applications smaller values (close to 0·1) have generally been found to yield the best results. This is partly due to the fact that, almost invariably, a certain amount of numerical diffusion adds itself to the 'physical' subgrid viscosity $\nu_s$. The choice of $c_s$ is discussed, among others, by Mason and Callen.[10] For the present simulations, the value 0·08 was chosen on the basis of former experience.[6,7] Further remarks are in Section 4.2.

The subgrid thermal diffusivity, $\alpha_s$, was modelled simply by

$$\alpha_s = \nu_s/\sigma_s, \tag{7}$$

$\sigma_s$ being a 'subgrid Prandtl number'. Equation (7) is the subgrid analogue of $\alpha_T = \nu_T/\sigma_T$, used in conventional turbulence modelling. However, while a value of $\sim$0·9 is generally accepted for the 'turbulent Prandtl number' $\sigma_T$, a wide range of values have been used by various authors for $\sigma_s$ in LES heat transfer predictions, from[11] 0·25 to[12] 0·5 and[13] 0·8. The smallest value (0·25) was found here to yield the best agreement with known temperature profiles. The rationale for a subgrid Prandtl number much smaller than unity is that pressure fluctuations may inhibit momentum transfer with respect to transfer of a scalar quantity at the subgrid scales.[14]

### *2.2. Computational domain and boundary conditions*

The computational domains for the plane-channel and the ribbed-channel cases are shown in Figure 1. Periodic boundary conditions were imposed along the streamwise direction ($x$) and the spanwise direction ($z$). The periodicity assumption requires that the extent of the computational domain along $x$ and $z$ must be larger than the characteristic lengths at which correlations between fluctuating quantities become negligible. For plane channels, experimental data by Comte-Bellot[15] suggest these lengths to be $\sim 3\delta$ streamwise and $\sim 1{\cdot}6\delta$ spanwise, $\delta$ being the channel half-height ($=H/2$, Figure 1). Thus, the values $L = 6\delta$ and $W = 4\delta$ were chosen. The same sizes were used for the ribbed channel, although no experimental data on correlation lengths were available for this geometry. The values chosen for the pitch-to-height ratio of the ribs, $P_1/h$, and for the blockage ratio of the channel, $h/H$, were 7·2 and 1/4·8, respectively. The former value, as discussed in Section 3.2, is the one of greatest engineering interest, as it has consistently been found empirically to yield the greatest enhancement of heat transfer rates. The size of the computational box is such that it includes two complete pitches; this allows direct testing of flow periodicity and improves statistics on computed quantities. A reduced computational domain, including only one rib and thus having $L = 3\delta$, was also used for grid and Reynolds number dependence assessment, see Section 4.3.

The issue of wall boundary conditions for large-eddy simulations of turbulent flows is discussed, for example, by Piomelli *et al.*[16] In this context, it was decided early on in the work that it was substantially preferable to use no-slip, rather than synthetic, wall boundary conditions.

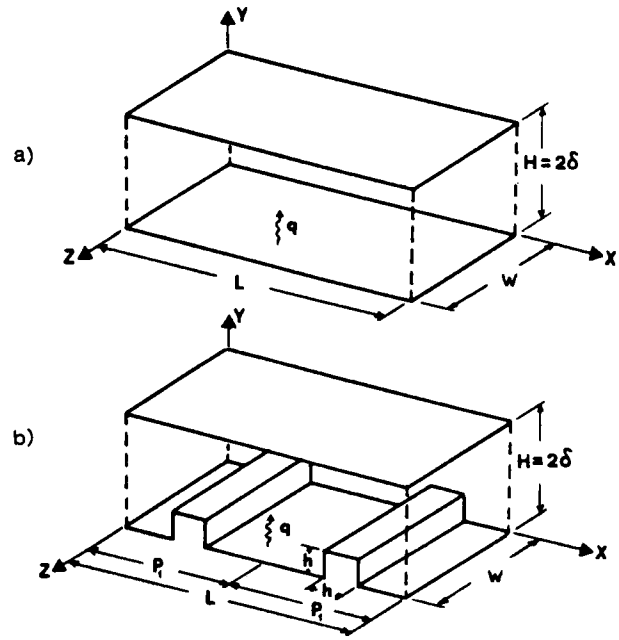


Figure 1. Schematic of the computational domains for: (a) the plane channel and (b) the ribbed channel

These can be applied equally well to geometrically complex as to simple flows; however, it is necessary to resolve the viscous-conductive sublayer by at least one grid point, which restricts the simulations to relatively low Reynolds numbers. Work on more complex boundary conditions, suitable for high-Reynolds-number flows, is in progress and will be reported in future papers.

The thermal boundary conditions were as follows:

(a) The top wall was adiabatic for both geometries.
(b) On the bottom wall, a constant heat flux $q$ was imposed in the plane-channel case. For the ribbed channel, the same heat flux $q$ was imposed on the horizontal wall between ribs, but a value $q/3$ on each face of a rib. Thus, the total heat input into the channel was the same for the plane and the ribbed ducts.

As streamwise periodicity is imposed, the computed pressure and temperature fields cannot be the 'true' ones, but periodic fields $P^*$, $T^*$ related to $P$ and $T$ by

$$P^* = P - (\mathrm{d}\hat{p}/\mathrm{d}x)x, \tag{8}$$

$$T^* = T - (\mathrm{d}\hat{T}/\mathrm{d}x)x, \tag{9}$$

where $\mathrm{d}\hat{p}/\mathrm{d}x\,(<0)$ and $\mathrm{d}\hat{T}/\mathrm{d}x\,(>0)$ are the mean streamwise pressure and temperature gradients. In order to compute $P^*$ and $T^*$ rather than $P$ and $T$, the following source terms must be added to the right-hand side of equations (2) (written for the direction $x$) and (3), respectively:

$$S_u = |\mathrm{d}\hat{p}/\mathrm{d}x|/\rho, \tag{10}$$

$$S_T = -q/(2\delta\rho C_p)u/\hat{u}. \tag{11}$$

Equation (11) is derived on the basis of the assumption $\partial\alpha_s/\partial x \ll u$; see Reference 6. Here $u$ is the local streamwise velocity and $\hat{u}$ the cross-section-averaged velocity, $\dot{M}/WH$.

For both the plane and the ribbed channel cases, the pressure drop per unit length $|\mathrm{d}\hat{p}/\mathrm{d}x|$ is imposed, while the flow rate (and, thus the Reynolds number) follows as a result of the computation.* A *mean* wall shear stress can be defined as

$$\tau = \delta\,\mathrm{d}\hat{p}/\mathrm{d}x, \tag{12}$$

and the corresponding mean friction velocity computed:

$$u_\tau = (|\tau|/\rho)^{1/2}. \tag{13}$$

This can be used to define dimensionless quantities as

$$y^+ = yu_\tau/\nu, \tag{14a}$$

$$u^+ = u/u_\tau, \tag{14b}$$

$$k^+ = k/u_\tau^2, \tag{14c}$$

$$p^+ = p/(\rho u_\tau^2), \tag{14d}$$

$$T^+ = (T_w - T)\rho C_p u_\tau/q, \tag{14e}$$

in which $T_w$ is the wall temperature at the nearest heated-wall location and $q$ the corresponding heat flux.

Equation (14a), in particular, is used to scale $y$ for use in the near-wall damping function (6). It should be observed that, in the ribbed channel, $\tau$ is the mean shear stress on the smooth wall and *not* on the ribbed wall. Thus, scaling $y$ by $u_\tau/\nu$ in equation (6) is not really appropriate, although it is the simplest choice; see Reference 7 for a discussion of the problem.

### 2.3. *Initial conditions*

Initial conditions were imposed as follows.

First, the *nominal* mean (cross-section-averaged) velocity $u^0$ was determined so that the *nominal* Reynolds number, based on $D_e$ (the hydraulic diameter $=4\delta$) was $Re^0 = 20\,000$ for both geometries. The required pressure gradient $|\mathrm{d}\hat{p}/\mathrm{d}x|$ was determined by

$$|\mathrm{d}\hat{p}/\mathrm{d}x| = (4C_f/D_e)\rho(u^0)^2/2 \tag{15}$$

in which the friction coefficient $C_f$ was expressed as follows.

(a) For the plane (smooth) channel, by using the correlation proposed by Beavers and Sparrow[17]

$$C_{f,sm} = 0{\cdot}127\ Re^{-0{\cdot}3} \tag{16}$$

valid for fully developed turbulent flow in flat ducts at moderate Reynolds numbers.

(b) For the ribbed channel, by using the friction multiplier proposed by Rapier:[18]

$$C_f/C_{f,sm} = 1 + 115\,h/D_e, \tag{17}$$

in which the hydraulic diameter, $D_e$, was expressed as twice the channel height $H$. According to equation (17) the required pressure drop was $\sim 13$ times higher in the ribbed duct ($h/D_e = 1/9{\cdot}6$) than in the plane channel.

* For this reason, we found it quite difficult to make predictions for a given $Re$.

Now, the mean velocity $u$ (along $x$) was set equal to $u^0$, and mean $v$ and $w$ were set equal to zero; random $u$, $v$ and $w$ fluctuations, having rms values equal to $u_\tau$, were distributed normally in the channel in order to trigger turbulence.

More sophisticated initial conditions are discussed in Reference 6; the exact form of them, however, has almost no influence on the flow development after some time. The initial temperature was set equal to zero throughout the channel.

### *2.4. Grid, time step and statistics*

Typical computational grids used had $32 \times 16 \times 16$ control volumes in the flow (along the $x$, $y$ and $z$ directions, respectively) for the plane channel, and $48 \times 24 \times 24$ for the ribbed channel. Slices of these grids parallel to the $x$–$y$ plane are shown in Figure 2. Grids were selectively refined near the walls, so that the viscous sublayer ($y^+ < \sim 11$) was resolved by at least one grid point in both geometries; they were uniformly spaced along $z$ and, for the plane channel, also along $x$. The dependence of results on the number of grid points is discussed in Sections 4.2 and 4.3. For the plane-channel case, different sizes of the computational domain, and different grids and Reynolds numbers, were also tested in preliminary runs; results are reported in References 6 and 7.

The time step was set at 1/100 of a LETOT ($\delta/u_\tau$) on the basis of former experience.[6] Simulations were run for 20 to 40 LETOTs, i.e. 2000–4000 time steps. With the grids of Figure 2, the maximum 'cell Reynolds number' ($u\Delta x/\nu$) was about $10^3$ and the maximum Courant number ($u\Delta t/\Delta x$) slightly less than unity.

Mean and fluctuating components of the (resolved) flow and temperature fields were computed by processing instantaneous fields as follows (see also Nomenclature). For any scalar $Q$, $\langle Q \rangle$ denotes the space average over the plane parallel to walls (plane channel) or over the duct's span (ribbed channel); $\langle \bar{Q} \rangle$ denotes the time average of $\langle Q \rangle$, generally taken over the last 5 or 10

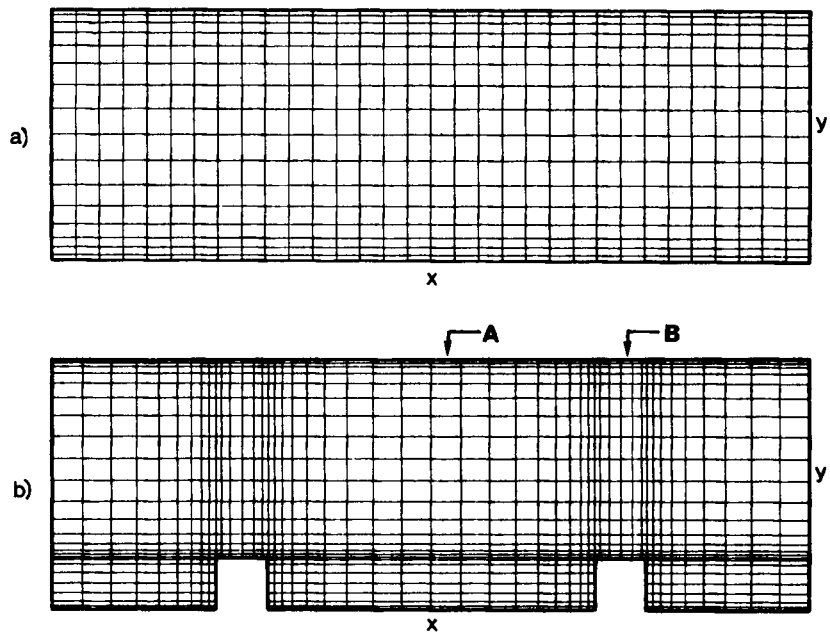


Figure 2. Computational grids in the $x$–$y$ plane for: (a) the plane channel and (b) the ribbed channel

LETOTs, i.e. over 500–1000 time steps. Similarly, $Q''_{rms} = \langle (Q - \langle Q \rangle)^2 \rangle^{1/2}$ denotes the root mean square of the fluctuating component of $Q$ with respect to a plane or a span; and $\bar{Q}''_{rms}$ is the time average of this over 5 or 10 LETOTs. Note that $\langle \bar{Q} \rangle$ and $\bar{Q}''_{rms}$ are one-dimensional fields (functions of the cross-stream co-ordinate $y$ only) in the plane-channel case, and two-dimensional fields (functions of $x$ and $y$) for the ribbed channel. Mixed moments (Reynolds stresses and heat fluxes) and wall quantities can be defined similarly. All quantities are considered in their dimensionless form equations (14).

### *2.5. Numerical methods and computational remarks*

The subgrid model described in Section 2.1 was implemented as discussed in Reference 19 in the computer code Harwell-FLOW3D, Release[3] 2.1. This is a finite difference code, using a centred (collocated) grid approach in conjunction with the Rhie–Chow algorithm[20] to prevent 'chequerboard' oscillations. Body-fitted grids can be used, although all simulations described here employ Cartesian, non-uniform grids (see Section 2.4). Details of the implementation of the Rhie–Chow method are given in Reference 21.

The code includes a number of options concerning differencing scheme, time stepping, pressure–velocity coupling, and linearized equation solvers. In the present simulations central differencing in space was used. Preliminary accuracy studies by Gavrilakis[22] with FLOW3D had shown that for LES applications only this differencing scheme was suitable, other schemes (including first- and second-order upwind, hybrid upwind and QUICK) being too dissipative, i.e. leading to a rapid decay of fluctuations. Similar conclusions were reached by the present authors in previous high-accuracy 2D simulations of high-Reynolds-number transient laminar flows.[23,24]

With regard to the time-stepping algorithm, both the fully implicit backward and the Crank–Nicolson methods were tested. Preliminary runs revealed no significant difference in results between the two schemes. However, the Crank–Nicolson method was used in all final simulations as being, in principle, more accurate and less dissipative.

As to the pressure–velocity coupling algorithm, the non-iterative scheme PISO[25] was chosen, as preliminary tests showed that it was 3–4 times faster than the iterative scheme SIMPLE[26] in large-eddy simulation of turbulent flows (see Reference 6 for a discussion of the problem of defining accuracy in such computations). Both algorithms were used in their modified forms, PISOC and SIMPLEC, based on the work by VanDoormal and Raithby.[27]

The linearized momentum and energy equations were solved by using Stone's Strongly Implicit Procedure[28] in its three-dimensional form, while the pressure-correction equation was solved by using a conjugate-gradient method with incomplete Cholesky preconditioning.[29]

Simulations were run on the Harwell CRAY-2 and on the IBM 3090-180E or 3090-200J (without vector facility) of the University of Palermo. Computing times for a simulation lasting 4000 time steps (40 LETOTs) were about 90 m for the plane channel (with a grid $32 \times 24 \times 24$) and about 130 m for the ribbed channel (grid $48 \times 24 \times 24$) on the CRAY-2, and 4–8 times higher on the IBM 3090-200J. Corresponding storage requirements were about 10 Mbytes and 14 Mbytes, respectively (i.e. about 100 real locations per grid point in the limit of large grids).

## 3. REVIEW OF LITERATURE RESULTS

### *3.1. Plane channel*

Experimental data for both mean and fluctuating velocities in simple channel flows have been obtainable for many years.[15,30] Recent and accurate measurements in fully developed plane-

channel flows include those of Kreplin and Eckelmann,[31] who used oil in a duct having an aspect ratio of 3·59 at $Re_\delta \approx 3400$, and those of Hussain and Reynolds[32] for $Re_\delta \approx 10\,000$. Experimental cross-stream profiles of mean and fluctuating velocities, once expressed in wall units as $u^+$, $u_{rms}$ etc. exhibit only a weak dependence on the Reynolds number. From correlation (16) and equations (12)–(14) it follows that the cross-section averaged velocity expressed in wall units, $u^+$, should increase as $Re^{0.15}$ in full developed flow. However, the measured maximum (centre-line) mean velocity is about 18 both in[31] ($Re_\delta \approx 3400$) and in[32] ($\mathrm{Re}_\delta \approx 10\,000$). Fluctuation data do not exhibit a clear trend with $Re$;[15,31,32] the streamwise fluctuation $u^+_{rms}$ is the largest, with peaks of 2·3–2·8 near the walls, while peak values of $v_{rms}$ and $w_{rms}$ are lower and close to each other. Turbulence becomes more isotropic in the central region of the duct.

There are no comparably accurate measurements of mean and fluctuating temperatures for *thermally fully developed* non-isothermal flow. For example, the holographic–interferometry results of Lockett[33] include real-time interferograms showing time-dependent thermal eddies at Reynolds numbers of $10^4$–$10^5$, but are for a thermal development length of only a few channel heights. In fully turbulent, fully developed flow the Nusselt number, defined as

$$Nu = \frac{q}{T_w - \hat{T}} \frac{D_e}{\lambda} \tag{18}$$

(in which $T_w$ is the wall temperature and $\hat{T}$ the cross-section-averaged fluid temperature) is expected to increase as $Re^{0.8}$ as, for example, in circular ducts. From (12)–(14) it follows that the cross-section-averaged dimensionless temperature, $T^+$, should increase only as $Re^{0.05}$.

Large-eddy simulations of isothermal plane-channel flows are relatively numerous. Early results are due to Deardorff.[34] The most accurate simulations presented so far are those of Moin and Kim,[35] who used a simplified form of Schumann's subgrid model[36] and spectral methods on very fine grids having up to $64 \times 64 \times 128$ ($x \times y \times z$) nodes. Results from different subgrid models were compared by Horiuti.[37] The influence of the wall boundary conditions was investigated by Piomelli *et al.*[16] and the influence of $c_s$ by Mason and Callen.[10] The flow in the near-wall region was simulated directly by Azab and McLaughlin.[38]

Flow with heat transfer in a plane channel with one wall heated was simulated by Hunter *et al.*,[11] who also discussed the analogy between the time growth of the simulated thermal boundary layer and the space development of its physical counterpart in flows not yet fully developed. Preliminary results of large-eddy simulations in plane channels with heat transfer were also presented by the present authors in a previous paper.[39]

### 3.2. *Ribbed channels*

Turbulence promoters have been widely used in engineering to enhance heat transfer or mixing.[40] Periodic square ribs on one wall of a plane duct can be considered as representative of a more general class of turbulence promoters; they are also a basic geometry for the study of recirculating flows with separation and reattachment, and thus have been extensively studied both experimentally[41–55] and numerically.[56–61]

On the basis of these studies, it has been known for some time that the best results in terms of heat transfer enhancement are obtained for values of the pitch-to height ratio, $P_1/h$, of about 7. For smaller values a single recirculation bubble is formed in the cavity between consecutive ribs and heat transfer is impaired, while for larger values the effect of the ribs is excessively 'diluted'. Maxima of local heat transfer are obtained in the reattachment region on the bottom wall and on the leading edge of each rib, in correspondance with flow impingement.

For the pitch-to-height ratio of 7·2, according to Rapier[18] pressure drop data are correlated by equation (17), and heat transfer data by

$$Nu = \text{const} \times Re^{0.7} \times (2{\cdot}4 + 20h/D_e). \tag{19}$$

From equations (17), (18) and (12)–(14) it follows that the channel-averaged dimensionless mean velocity, $u^+$, and mean temperature, $T^+$, should both increase as $Re^{0.15}$.

Most of the computational results presented for this geometry were based on the $k$–$\varepsilon$ turbulence model. LES results for the flow over periodic obstacles were presented by Fodemski *et al.*,[62] who used a spectral code with co-ordinate transformation. The shape of the obstacles could be changed progressively from smooth to square; an unconditional instability occurred when the sharpness of the geometry exceeded a certain limit. LES results for square ribs at a Reynolds number of $\sim 10^4$ were presented by Kobayashi *et al.*[13] They were obtained with a finite difference approach and a three-dimensional grid having about 9000 nodes; the computational domain included a single rib. The rib pitch-to-height ratio, $P_1/h$, was five and a single 'trapped' recirculation bubble was predicted. These results include heat transfer predictions and are compared with $k$–$\varepsilon$ results[13] but not with experimental data.

## 4. RESULTS AND DISCUSSION

### *4.1. Turbulence energy and flow rate*

The behaviour of the channel-averaged resolved turbulence energy is shown in Figure 3 for both geometries and for $Re^0 = 20\,000$, $c_s = 0.08$, grids $32 \times 16 \times 16$ (smooth channel) or $48 \times 24 \times 24$ (ribbed channel). In the smooth channel case, $k^+$ decays rapidly as the initial flow field (which does *not* satisfy continuity) is replaced by a mass-conserving flow, and then increases

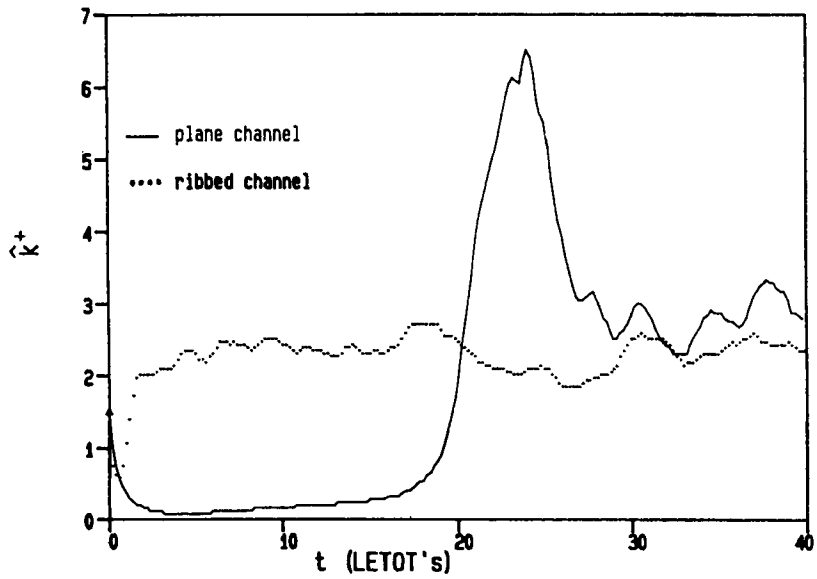


Figure 3. Resolved turbulent kinetic energy, averaged over the whole channel and expressed in wall units, as a function of time in LETOTs for the plane and the ribbed channels at $Re^0 = 20\,000$

very slowly for many LETOTs as a boundary layer grows, and vorticity is built up near the walls. It then increases steeply, overshoots and finally reaches a statistically stationary value of about 2·5. For the ribbed channel, the low-turbulence phase is much shorter ($\sim 1$ LETOT), no overshoot occurs, and an asymptotic behaviour is established after a few LETOTs.

In both cases, the instantaneous Reynolds number increased slowly starting from the initial (nominal) value of 20 000. The exact behaviour of both $k^+$ and $Re$ was found to be sensitive to the constant $c_s$ and to the grid used. For the ribbed channel, the final $Re$ (LETOTs 30–40) was 26 600, i.e. the flow rate was overpredicted by 33 per cent with respect to correlations (11) and (13). The corresponding $\delta$-Reynolds number was $\sim 6650$. Smaller overpredictions were obtained for the smooth-channel case; see the next section.

### *4.2. Detailed results—smooth channel*

Grid dependence could be investigated only to a limited extent, due to CPU time and storage limitations. The numbers of streamwise, cross-stream and spanwise grid points, $N_x$, $N_y$, $N_z$, were varied individually in the ranges 24–48, 16–32 and 12–24, respectively, for $Re^0 = 20\,000$ and $c_s = 0{\cdot}08$.

The influence of the streamwise resolution was found to be negligible in this range. The effect of varying $N_y$ and $N_z$ is summarized in Figures 4 and 5, respectively. Cross-stream profiles of the mean velocity $\langle \bar{u} \rangle$ (a), and of the streamwise fluctuation $\bar{u}''_{\mathrm{rms}}$ (b), are reported in wall units for $N_y = 16$, 24 and 32 in Figure 4 (for fixed $N_x = 32$, $N_z = 16$) and for $N_z = 12$, 16 and 24 in Figure 5 (for fixed $N_x = 32$, $N_y = 16$).

It is clear from Figure 4(a) that increasing the cross-stream resolution from 16 to 24 grid points reduces the mean velocity significantly, while a further increase to 32 points produces only a small effect. Peak values of the streamwise fluctuating velocity, Figure 4(b), increase slightly with $N_y$ as a larger fraction of the total turbulent fluctuations is 'captured' at the resolved scale. Similar results are obtained for the other two fluctuating components. Temperature values are influenced by $N_y$ less than velocity profiles; $T^+$ decreases by about 3 per cent for $N_y$ increasing from 16 to 32.

From Figure 5 it can be seen that also an increase in $N_z$ from 12 to 16 reduces the mean velocity significantly; a further increase to 24 points has but a small effect. Fluctuation profiles are little affected by the number of spanwise grid points; for increasing $N_z$ peak values of $u''_{\mathrm{rms}}$ increase slightly and move towards the walls, while its levels decrease in the bulk flow region. Temperature values increase slightly ($\sim 5\%$) for $N_z$ increasing from 12 to 24.

It has to be added that increasing the number of grid points in any direction resulted in a significant increase of the duration of the low-turbulence phase shown in Figure 3; for $N_y$ or $N_z$ equal to 24, $\hat{k}$ was still very low after 40 LETOTs, unless very small values of the Smagorinsky constant $c_s$ were used. Thus, in order to obtain self-sustaining turbulence it was necessary to start the simulations not from the initial conditions described in Section 2.3, but from the output of a preliminary 20-LETOT simulation at $c_s = 0$.

Reynolds number dependence was investigated only in the limited range $Re^0 = 10\,000$ to 40 000. At higher Reynolds numbers the near-wall resolution would be insufficient to have at least one grid point in the viscous sublayer, and 'synthetic' wall boundary conditions would be needed (several of these are currently being tested and results will be reported in future papers). On the other hand, at lower Reynolds numbers the flow would not be fully turbulent, and the use of the Smagorinsky subgrid model would not be appropriate.

For the range examined, results are summarized in Figure 6: cross-stream profiles of the mean velocity $\langle \bar{u} \rangle$ and of the mean temperature $\langle \bar{T} \rangle$ expressed in wall units, equations (14), are reported for $Re^0 = 1$, 2 and $4 \times 10^4$ and for a $32 \times 24 \times 16$ grid. Examination of these profiles

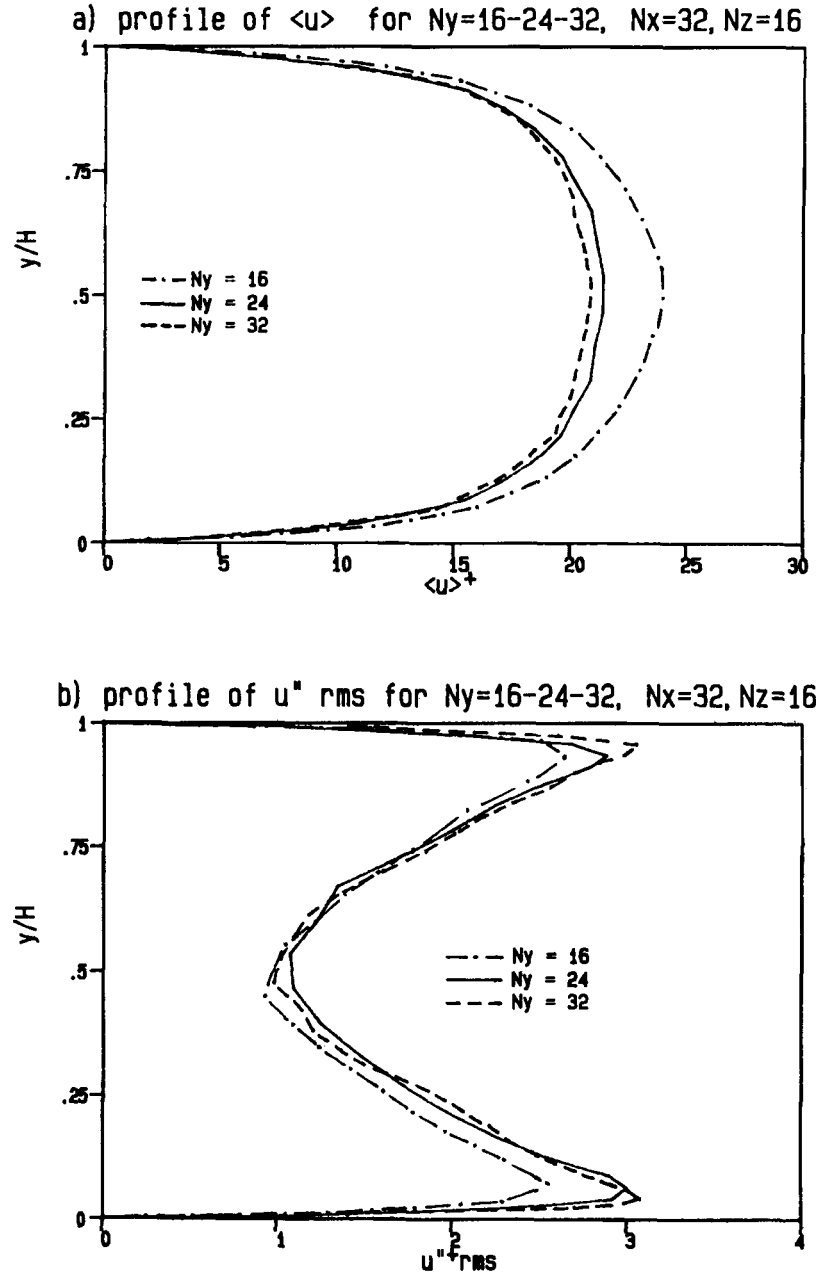


Figure 4. Plane channel: comparison of cross-stream profiles of $\langle \bar{u} \rangle$ and $\bar{u}''_{rms}$ (in wall units) for $N_y$ varying from 16 to 32 and $N_x = 32$, $N_z = 16$ ($Re^0 = 20\,000$)

reveals that the use of 'wall units' makes the mean flow and temperature fields little dependent on $Re$. Predicted values of $\hat{u}^+$ and $\hat{T}^+$ vary approximately as $Re^{0.12}$ and $Re^{0.06}$; as discussed in Section 3.1, the trends suggested by experimental data are $Re^{0.15}$ and $Re^{0.05}$, respectively. A similar weak dependence on $Re$ is obtained also for the resolved fluctuations.

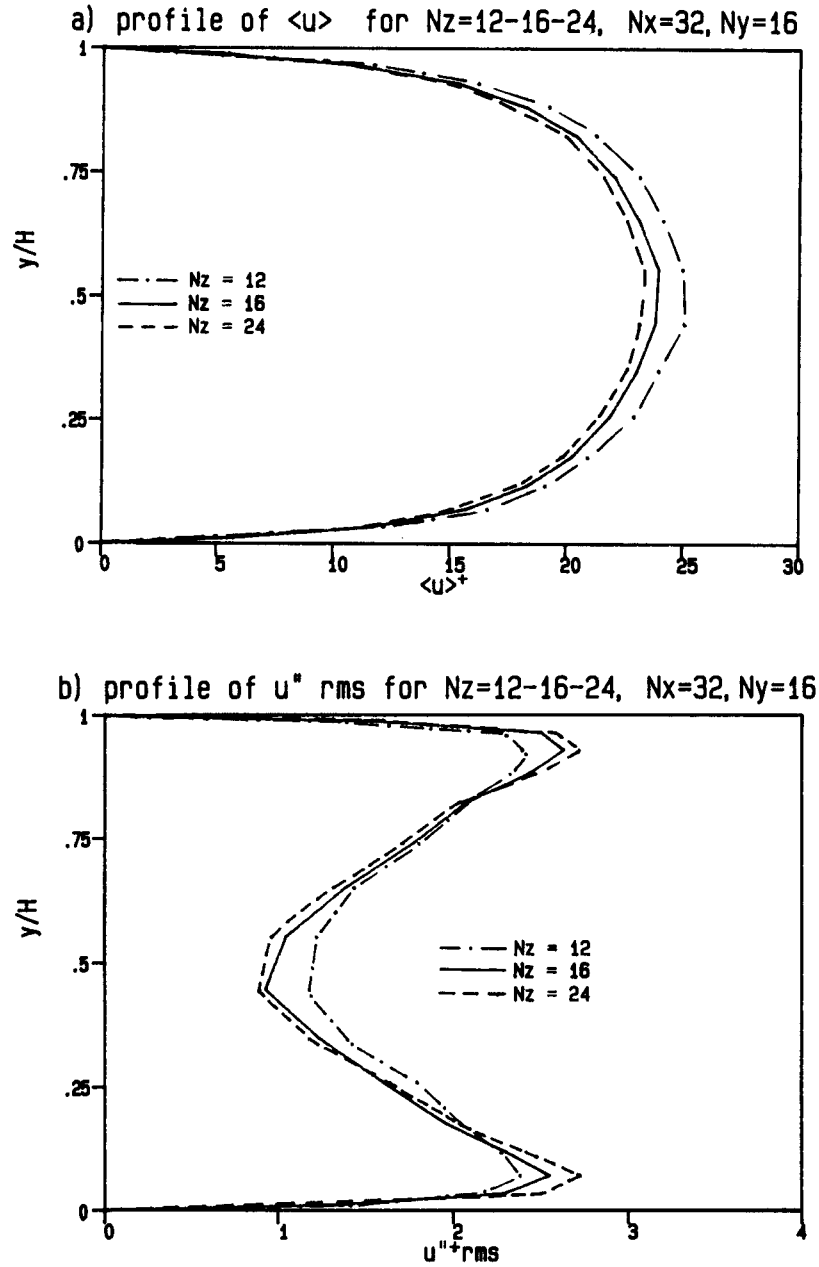


Figure 5. Plane channel: comparison of cross-stream profiles of $\langle \bar{u} \rangle$ and $\bar{u}''_{rms}$ (in wall units) for $N_z$ varying from 12 to 24 and $N_x = 32$, $N_y = 16$ ($Re^0 = 20\,000$)

Results of a 'reference' simulation at $Re^\circ = 20\,000$ ($Re^\circ_\delta = 5000$) using $32 \times 24 \times 24$ grid points along $x$, $y$ and $z$ and $c_s = 0{\cdot}08$ are reported below.

Cross-stream profiles of mean and rms fluctuating quantities are shown in Figures 7–12. All mean and rms values are taken over planes parallel to the walls, and further averaged in time over

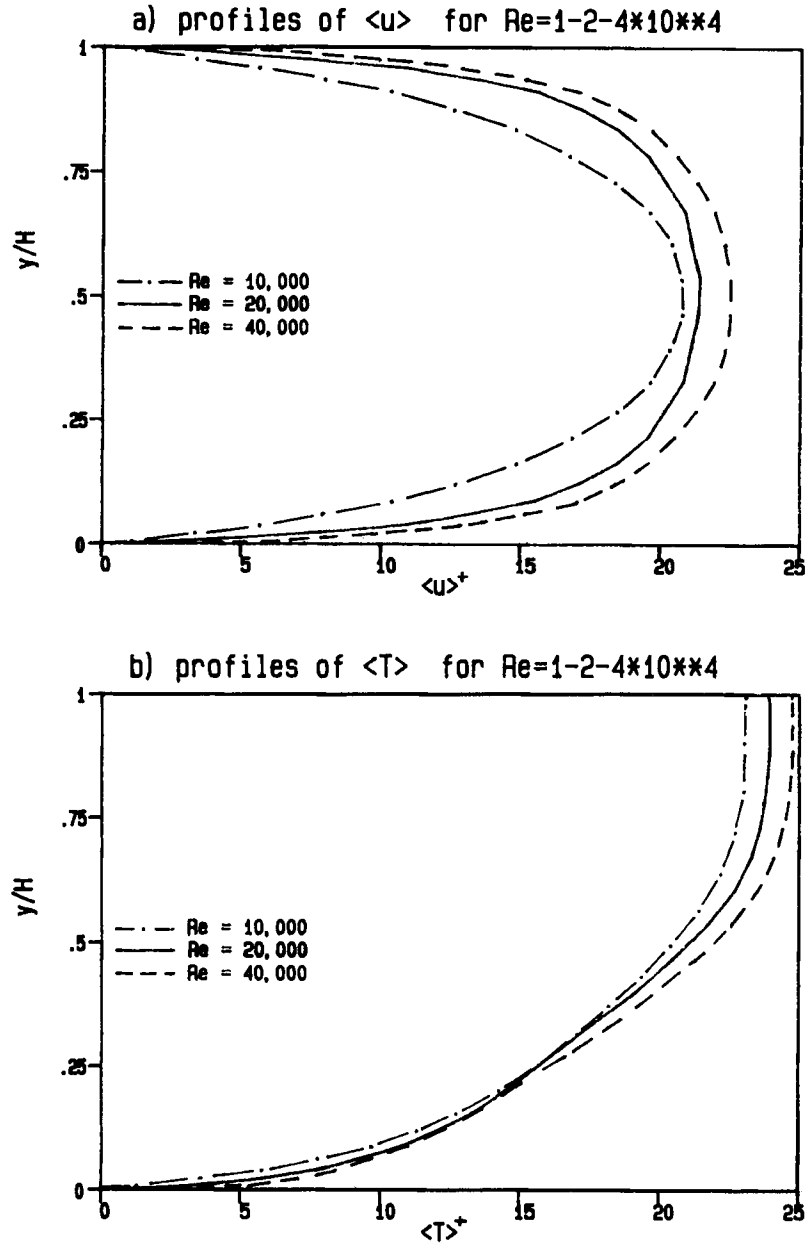


Figure 6. Plane channel: comparison of cross-stream profiles of $\langle \bar{u} \rangle$ and $\langle \bar{T} \rangle$ (in wall units) for different Reynolds numbers and a $32 \times 24 \times 16$ grid

LETOTs 30 to 40. The imposed pressure gradient was computed from equations (15) and (16). Results are compared with the available experimental data of Kreplin and Eckelmann[31] ($Re_\delta \approx 3400$) and of Hussain and Reynolds[32] ($Re_\delta \approx 10\,000$). Also reported are LES predictions by Moin and Kim[35] ($Re_\delta \approx 10\,000$), and $k$–$\varepsilon$ results obtained with Harwell-FLOW3D for the same imposed pressure gradient as in LES.

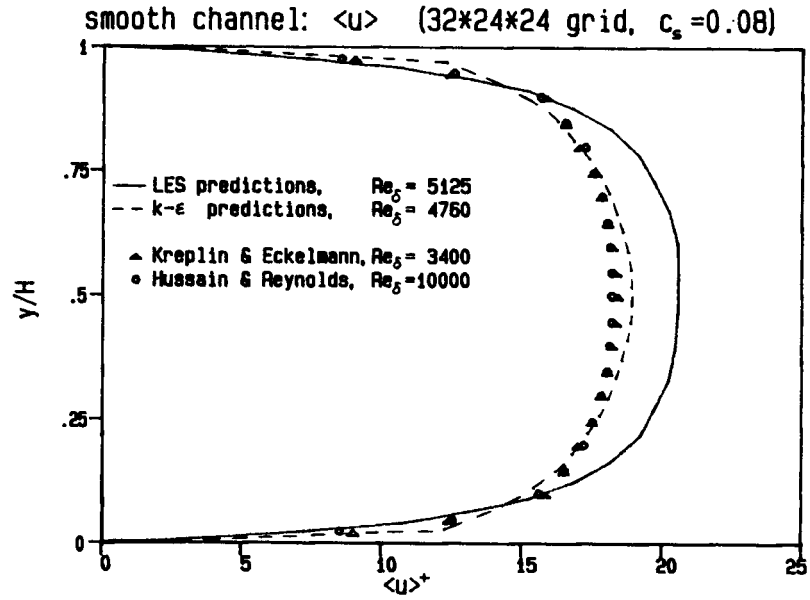


Figure 7. Plane channel: comparison of computed and experimental cross-stream profiles of the mean velocity, $\langle \tilde{u} \rangle$ in wall units). Values of the $\delta$-Reynolds number are indicated

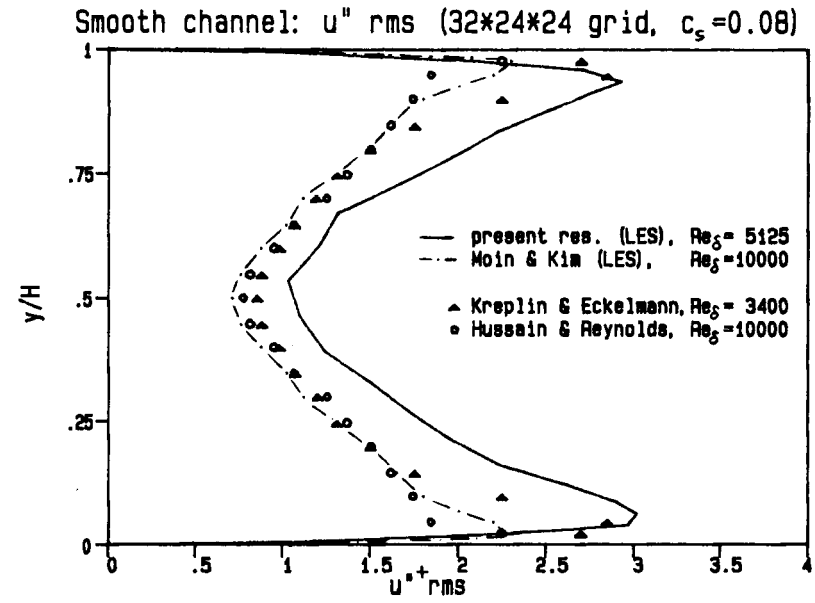


Figure 8. Plane channel: comparison of computed and experimental cross-stream profiles of the streamwise velocity fluctuation, $\tilde{u}''_{rms}$ (in wall units). Values of the $\delta$-Reynolds number are indicated

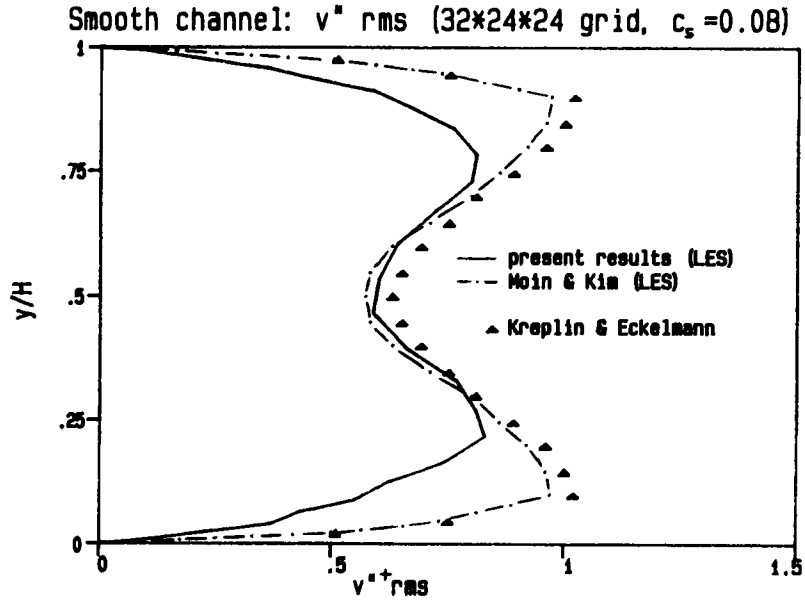


Figure 9. Plane channel: comparison of computed and experimental cross-stream profiles of the cross-stream velocity fluctuation, $\tilde{v}''_{rms}$ (in wall units). Values of the $\delta$-Reynolds number are indicated

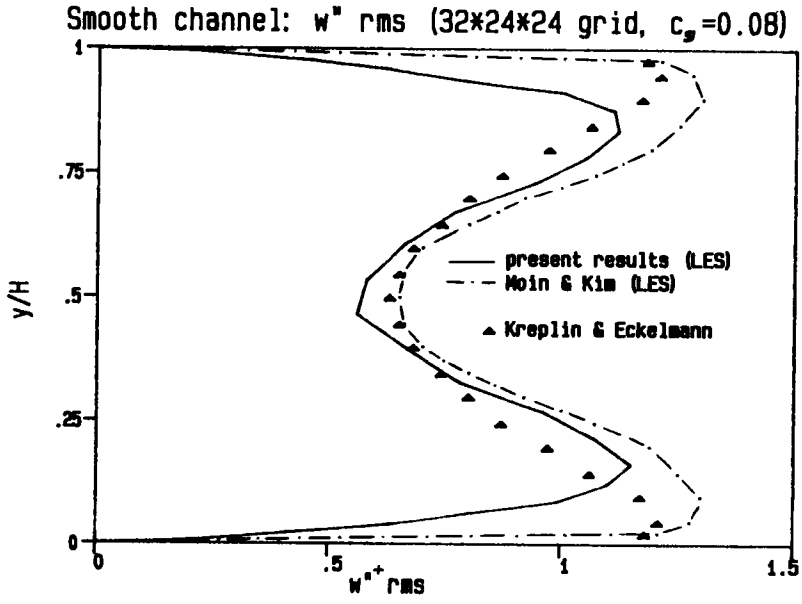


Figure 10. Plane channel: comparison of computed and experimental cross-stream profiles of the spanwise velocity fluctuation, $\tilde{w}''_{rms}$ (in wall units). Values of the $\delta$-Reynolds number are indicated

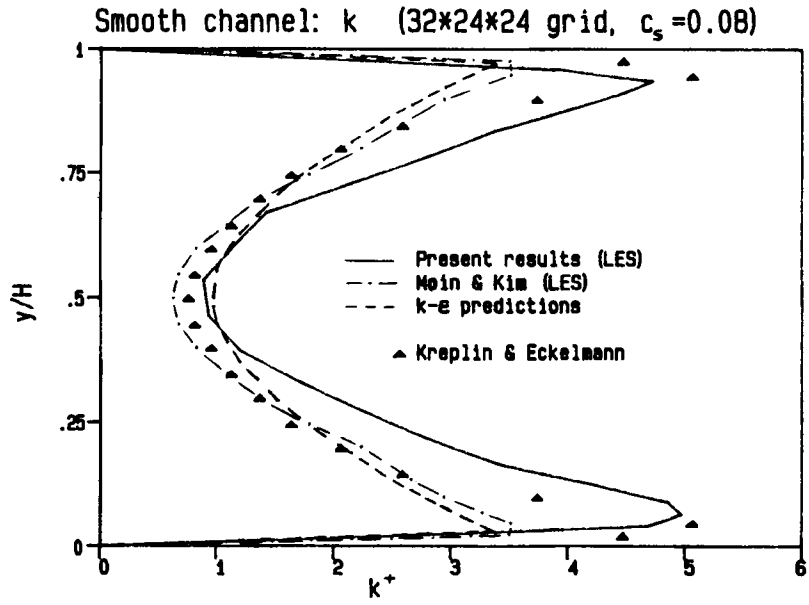


Figure 11. Plane channel: comparison of computed and experimental cross-stream profiles of the turbulent kinetic energy, $\langle \bar{k} \rangle$ (in wall units). Values of the $\delta$-Reynolds number are indicated

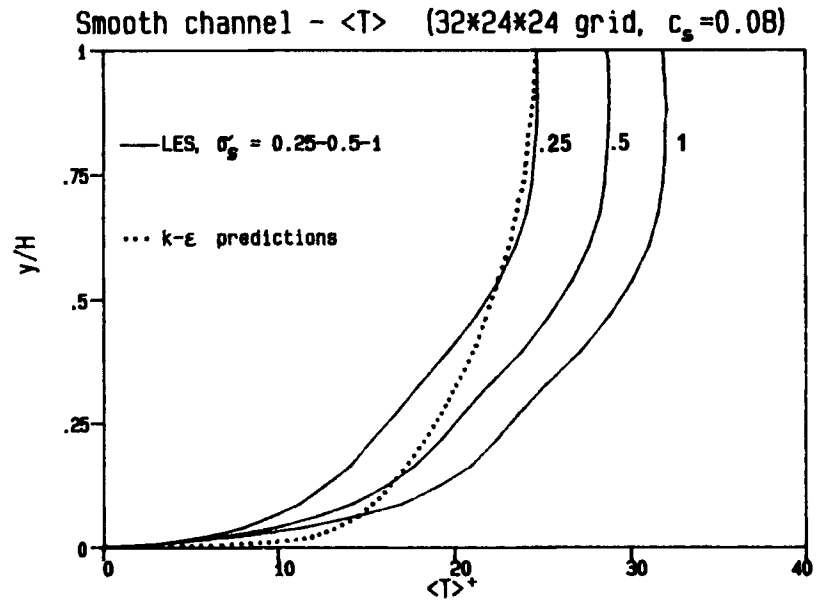


Figure 12. Plane channel: cross-stream profiles of the mean temperature $\langle \bar{T} \rangle$ (in wall units) for different values of the subgrid Prandtl number $\sigma_s$, and comparison with $k$-$\varepsilon$ predictions ($Re^0 = 20\,000$)

The mean velocity profile, Figure 7, is only slightly overpredicted by LES; the Reynolds number between LETOTs 30 and 40 was $\sim 20\,500$. Note that, if the $32 \times 16 \times 16$ results are plotted, Figure 4(a), a much larger overprediction is obtained, comparable to that obtained by Deardorff[34] using a similar number of grid points ($\sim 6700$). Thus, insufficient resolution of the computational domain appears to be the most likely cause for overpredictions of $\hat{u}$ and $Re$. In Reference 6, it was found that $Re$ decreased for increasing values of $c_s$; with the coarse $32 \times 16 \times 16$ grid, a value of 0·05 yielded a much worse overprediction, while a value of 0·10 gave a better agreement with the known results. However, using values of $c_s$ of 0·10 or larger led to unrealistic results as regards the fluctuation profiles and the predicted near-wall structures ('streaks').

The fluctuation profiles predicted for $c_s = 0{\cdot}08$ with the $32 \times 24 \times 24$ grid, Figures 8–10, are on the whole satisfactory. The only reservation applies to that of the cross-stream component, $v''_{rms}$, which exhibits peaks too flat and far from the walls. This is probably due to poor resolution of the near-wall region; there is only one grid point lying in the viscous sublayer $y^+ < 11$, against 3–4 points in Moin and Kim's simulations.

Levels of the total (resolved) kinetic energy of the turbulence, Figure 11, compare favourably with experimental data, while the $k$–$\varepsilon$ model appears to underpredict $k$.

Temperature predictions are heavily affected by the value chosen for the subgrid Prandtl number $\sigma_s$ in equation (7). Profiles of $\langle T \rangle$ computed for $\sigma_s = 0{\cdot}25$, 0·5 and 1 are reported in Figure 12. As mentioned in Section 3.1, the literature is poor in experimental results on *thermally fully developed* single-sided heat transfer in plane or rectangular channels, although this is a rather fundamental geometry. However, $k$–$\varepsilon$ predictions, based on wall functions and on Jayatilleke's correlations,[63] agree well with experimental data for similar geometries where these are available, and were assumed as reference results (broken line in Figure 12). It is evident that they are best approximated by the curve for $\sigma_s = 0{\cdot}25$; the same value was used by Hunter *et al.*[11] in previous LES predictions, and is lower than that (0·5) derived by Antonopoulos-Domis for isotropic turbulence.[12] However, even with this small value of $\sigma_s$ gradients of $\langle T \rangle$ are overpredicted in the central region of the channel, where turbulent fluctuations are lowest. This could be an inherent shortcoming of the simple gradient-diffusion model used here for the subgrid heat flux.[6]

One of the most mentioned aspects of turbulent channel flows in the context of LES are the coherent near-wall structures. Among them, the 'streaks'[64] are streamwise-elongated regions of high- and low-speed fluid, alternating in the spanwise direction. Their spacing is experimentally found to be $\sim 100$ in wall units, while their length is between 500 and 1000. These structures were predicted with good accuracy (with some overprediction of their spanwise spacing) by Moin and Kim,[35] who had four grid points within the viscous sublayer $y^+ < 11$, and by Azab and McLaughlin[38] by direct simulation of the near-wall region.

Figure 13(a)–13(c) shows contour plots of the instantaneous streamwise velocity $u$ on a plane $y^+ = 29$, for three different values of the subgrid model constant $c_s$ in equation (6). The simulations are for a nominal Reynolds number, $Re^0$, of 32 000, a $32 \times 16 \times 16$ grid, and a computational box having $L = 5\delta$ and $W = 3\delta$, i.e. smaller than that used for the results discussed above. The standard graphic post-processor of Harwell-FLOW3D, OUTPROC[65] was used. Thick lines indicate contours of the midrange (not average) velocity; the regions inside them are high-velocity portions of fluid.

For $c_s = 0{\cdot}05$, no clearly organized structure can be recognized. For $c_s = 0{\cdot}10$, on the other hand, streak length is so large that it exceeds the streamwise extent of the computational box ($\sim 2130$ wall units). Most realistic results are obtained for the intermediate value $c_s = 0{\cdot}08$. The span of the computational box is about 1280 in wall units; the streak spacing is about 400, much larger than the experimental value. Probably, this overprediction is mostly due to insufficient

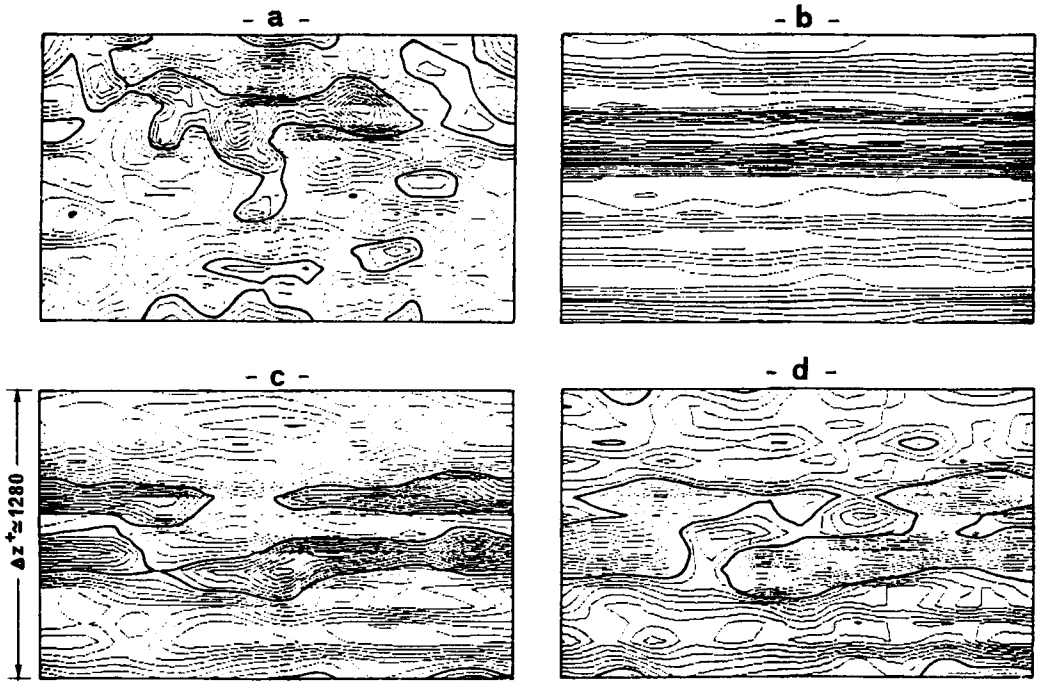


Figure 13. Plane channel: contour plots of instantaneous streamwise velocity, $u$, and temperature, $T$, on the plane $y^+ = 29$ for different values of $c_s$ ($Re^0 = 32\,000$): (a) $u$ contours, $c_s = 0{\cdot}05$; (b) $u$ contours, $c_s = 0{\cdot}10$ (c) $u$ contours, $c_s = 0{\cdot}08$; (d) $T$ contours, $c_s = 0{\cdot}08$

resolution of the near-wall region; simulations repeated for a lower Reynolds number ($Re = 10\,000$), with *two* grid points in the viscous sublayer, yield a streak spacing of about 100–150 wall units, only slightly overpredicted. However, part of the blame may be put on the subgrid model; Horiuti[37] compared LES channel flow predictions using the Smagorinsky model and a subgrid-energy transport model, and found that only the former led to overpredicting the spanwise streak spacing.

The dependence of the streak pattern on the constant $c_s$ has not, to the authors' knowledge, been reported previously. It shows that a certain minimum value of the subgrid viscosity is required to sustain the spatial correlations giving rise to these and similar coherent structures; if $c_s$ is too large, however, excessive streamwise correlation ensues, giving rise to overprediction of the streak length. No effect of $c_s$ on the spanwise streak spacing was found here.

Figure 13(d) shows the temperature contours corresponding to the streaks in Figure 13(c) for $c_s = 0{\cdot}08$. Not surprisingly, they exhibit the same general pattern as velocity contours, with high-temperature regions corresponding to low-speed fluid and *vice versa*.

### *4.3. Detailed results—ribbed channel*

For the ribbed channel, partial results have been reported in References 66 and 67. The investigation of grid dependence was more difficult here than for the smooth channel, see remarks in Section 4.2. The 48 × 24 × 24 grid shown in Figure 2(b) is close to the upper limits allowed by CPU time and storage (the CRAY-2 at Harwell would have allowed, in principle, grids having up

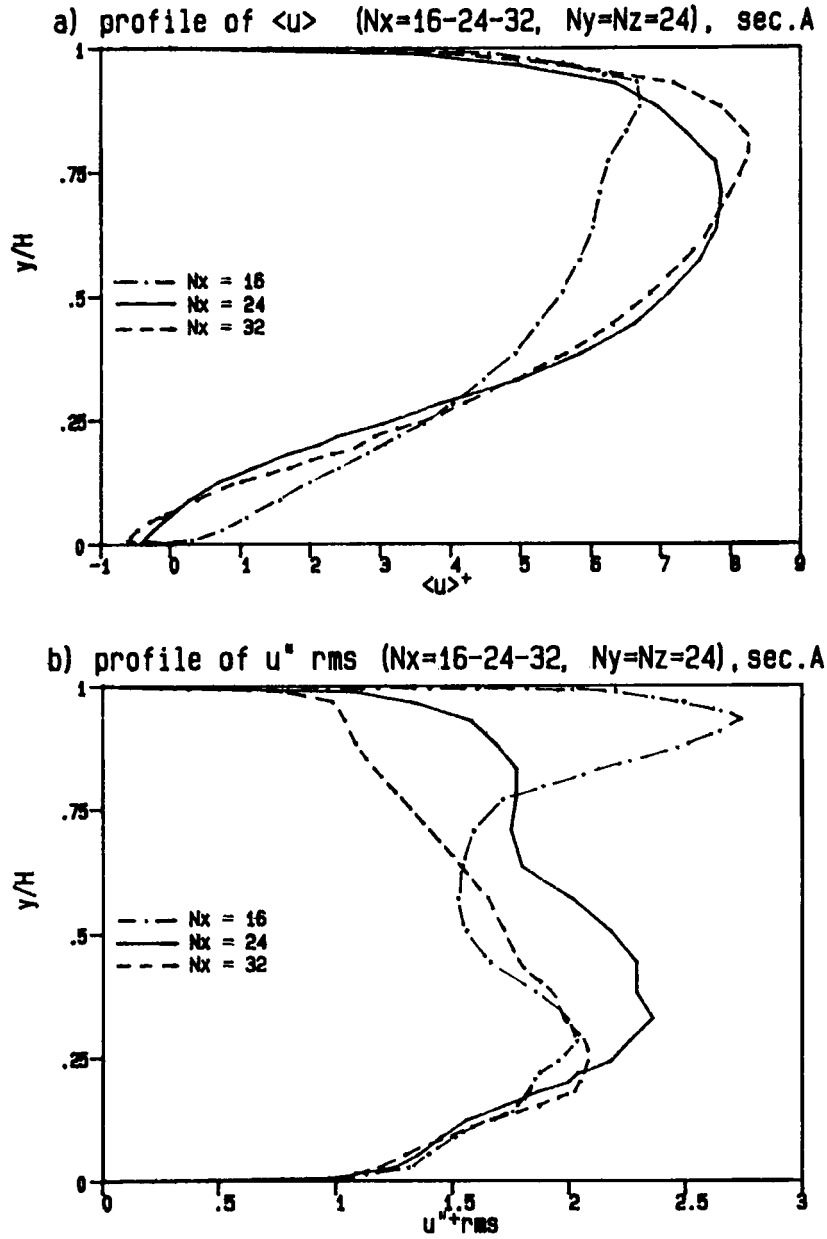


Figure 14. Ribbed channel: comparison of cross-stream profiles of $\langle \bar{u} \rangle$ and $\bar{u}''_{rms}$ (in wall units) at section A, Figure 2(b), for $N_x$ varying from 16 to 32 and $N_y = N_z = 24$ ($Re^0 = 20\,000$, only one rib included in computational domain)

to $\sim 10^6$ volumes, but only a limited CPU-time budget was available on it. On the other hand, on the IBM 3090 of the University of Palermo Computing Centre the time allowance was larger but only 16 Mbytes of in-core storage were available).

Due to these limitations, the sensitivity study was conducted by varying individually the number of streamwise, cross-stream and spanwise grid points, $N_x$, $N_y$ and $N_z$, in the range 16–32

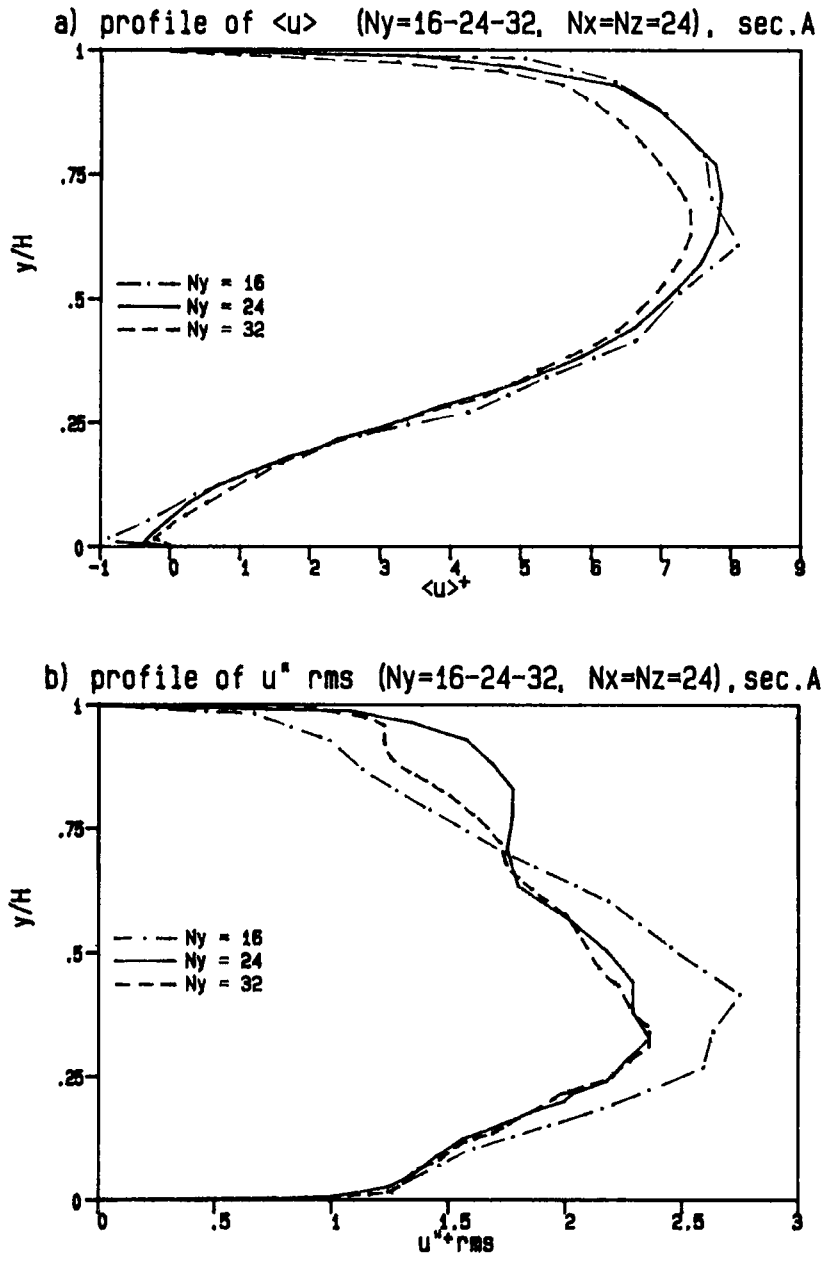


Figure 15. Ribbed channel: comparison of cross-stream profiles of $\langle \bar{u} \rangle$ and $\bar{u}''_{rms}$ (in wall units) at section A, Figure 2(b), for $N_y$ varying from 16 to 32 and $N_x = N_z = 24$ ($Re^0 = 20\,000$, only one rib included in computational domain)

for all directions, but for a 'reduced' computational domain including only one complete rib pitch. The number of spanwise points, $N_z$, was found here to have little influence on the results in the range examined. For varying $N_x$ and $N_y$, typical results are shown in Figures 14 and 15, respectively: cross stream profiles of $\langle u \rangle$ (a) and $\bar{u}''_{rms}$ (b), expressed in wall units, are reported for the channel cross section midway between consecutive ribs (section A in Figure 2(b)).

Figures 14 and 15 suggest that 24 cross-stream and streamwise points (per pitch) are sufficient to give a basically grid-independent flow field, including the backflow (recirculation) region downstream of a rib. An insufficient streamwise resolution ($N_x = 16$) results in failure to predict backflow at section A, Figure 14(a), and in unrealistically high fluctuations near the smooth wall, Figure 14(b). The cross-stream resolution appears to be less critical, Figure 15.

Comparison between simulations for a single rib and for two consecutive ribs did not evidence any significant difference in the results. However, final simulations were run for the two-rib domain shown in Figure 1(b) in order to improve statistics and to conform to the correlation-length considerations discussed in Section 2.2.

Reynolds number dependence was investigated in the restricted range $Re^0 = 10\,000$ to 40 000 for the same reasons discussed in Section 4.2. Results are summarized in Figure 16 for the section midway between consecutive ribs. As in Figure 6, cross-stream profiles are shown for $\langle u \rangle$ and $\langle T \rangle$, expressed in wall units. It is clear that, once made dimensionless, mean fields are little influenced by the Reynolds number. Predicted values of both $\hat{u}^+$ and $\hat{T}^+$ vary as $Re^{0.10}$ approximately. As discussed in Section 3.2, experimental correlations give for these quantities a dependence as $Re^{0.15}$.*

For the ribbed channel, an additional parameter which influences the flow and thermal fields is the blockage ratio, $h/H$. Due to the necessity of having an adequate cross-stream resolution in the rib region, and to limitations on the overall grid size, values of $h/H$ significantly less than the 'reference' one (1/4·8) could not be investigated in the present study. The flow and thermal fields in the proximity of a rib, as well as the shear stress, pressure and temperature distributions on the bottom wall, should be little affected by $h/H$.* However, it is clear that comparison with experimental results obtained for different values of this ratio has, strictly speaking, only a qualitative nature.

In the following, we concentrate on results for $h/H = 1/4{\cdot}8$, $Re^0 = 20\,000$ and a 48*24*24 grid, covering two ribs. They were obtained for $c_s = 0{\cdot}08$ and $\sigma_s = 0{\cdot}25$. An overall view of the instantaneous (resolved) flow and temperature fields is given by Figures 17–20.

Figure 17 shows the instantaneous velocity field on a plane ($y^+ = 11$) close to the ribbed wall. Vectors are ($u$, $w$); some contours of $v$ are superimposed. Large eddies rotating in the $x$–$z$ plane (i.e. strong three-dimensionality of the flow) and intense backflow regions near the leading sides of the ribs are the most apparent features.

Figure 18 is an instantaneous map of the shear stress on the bottom wall; black cells are those in which $\tau_w < 0$, i.e. forward (direct) flow occurs. The main reattachment regions at $\sim 2/3$ of the distance between ribs appear 'patchy', which confirms the strong three-dimensionality of the flow. Almost continuous black stripes downstream of each rib indicate that stable counter-rotating corner eddies occur below the main recirculation regions.

Figure 19 is a temperature map of the ribbed wall at the same instant, $t = 40$ LETOTs. Here, black regions are those where the wall temperature is *lower* than the plane average, i.e. higher heat transfer occurs. These are concentrated both in the proximity of reattachment areas and immediately upstream of each rib.

Figures 20(a) and 20(b) show instantaneous velocity and temperature fields at $t = 40$ LETOTs on an arbitrary plane $z =$ constant. Only the region near one rib is shown.

---

* A referee has helpfully pointed out that additional References 68–70 suggest a somewhat stronger dependence of $\hat{T}^+$ on $Re$. From their data we estimate such to be $\hat{T}^+ \sim Re^{0{\cdot}2-0{\cdot}3}$. Similarly, where we conclude $H/h$ not to affect $Nu$, rather less evidence from the references infers the same influence on $Nu$ of $h/H$, namely 0·2–0·3. We are grateful to the referee for these comments, and leave the question open, making the point that we were not seeking to resolve every issue.

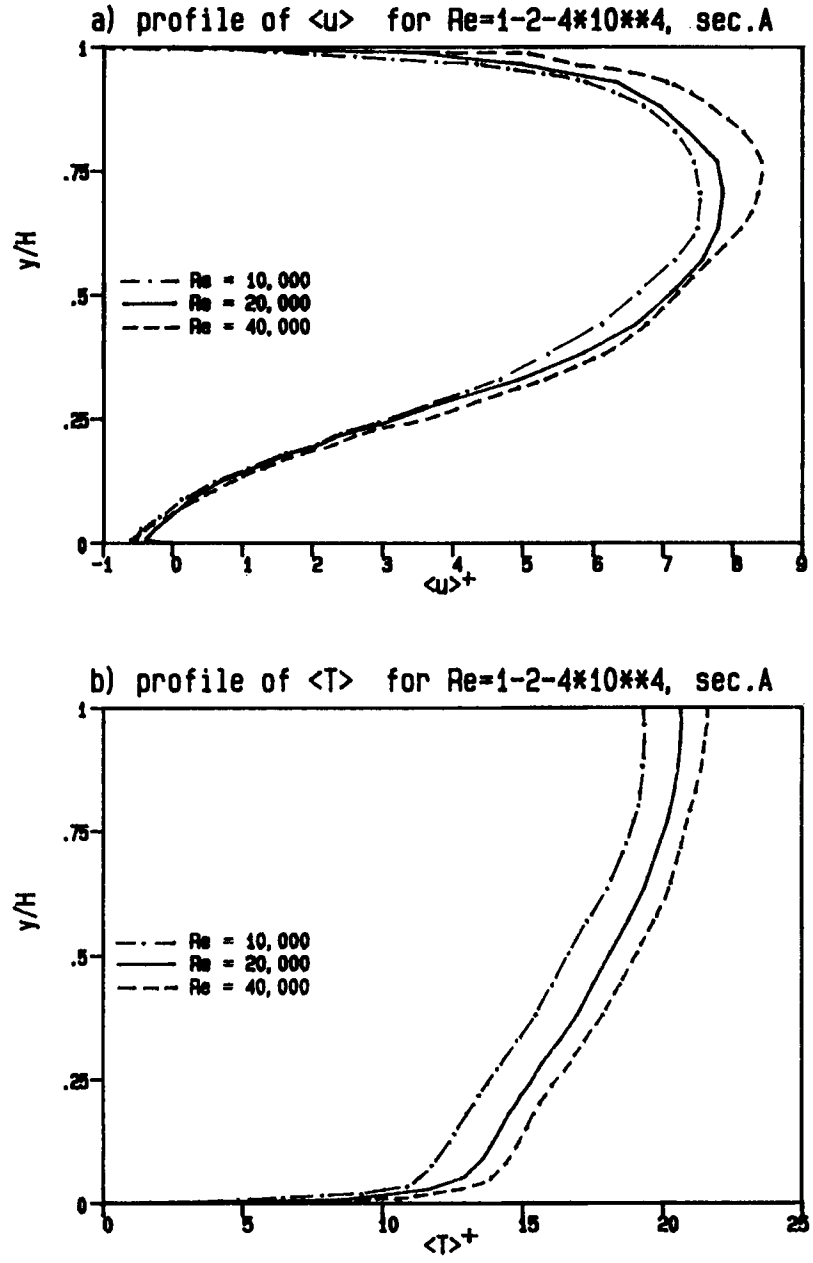


Figure 16. Ribbed channel: comparison of cross-stream profiles of $\langle \bar{u} \rangle$ and $\langle \bar{T} \rangle$ (in wall units) at section A, Figure 2(b), for different Reynolds numbers and a 24 × 24 × 24 grid (only one rib included in the computational domain)

The effect of spanwise averaging and time averaging on the predicted temperature field is shown in Figures 21(a)–21(c). The top graph (a) is a shade plot of the temperature field on the plane $z = W/2$ at the instant $t = 40$ LETOTs; some isotherms are depicted for purposes of clarity, and large irregular thermal structures are clearly visible. The central graph (b) is a plot of the

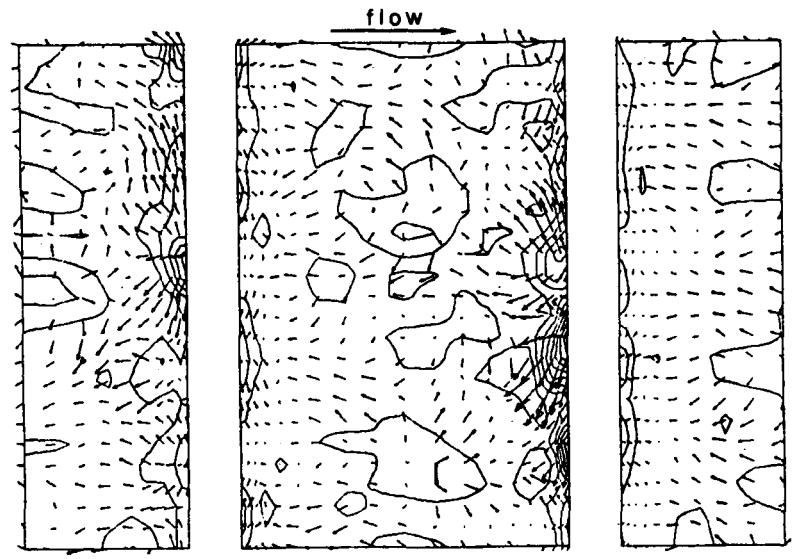


Figure 17. Ribbed channel ($Re^0 = 20\,000$): instantaneous velocity field on the plane $y^+ = 11$ parallel to the ribbed wall (vectors $u$–$w$, contours of $v$)

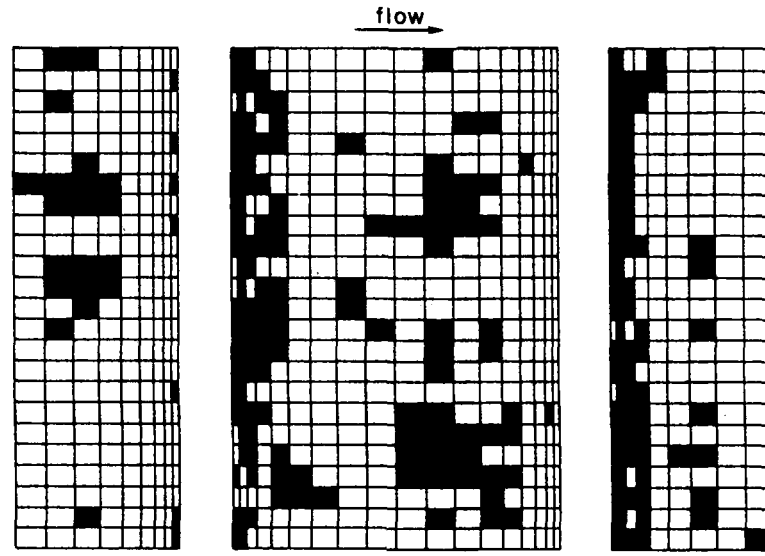


Figure 18. Ribbed channel ($Re^0 = 20\,000$): instantaneous shear stress map on the ribbed wall (dark cells indicate $\tau_x < 0$, i.e. forward, or direct, flow)

spanwise-averaged field at the same instant; large thermal eddies present in graph (a) have been smoothed away by spanwise averaging. Similar isotherm patterns are recorded by taking interferograms, which inevitably average the temperature field over the channel span.[71] The problem for extracting information about the flow structure from similar interferograms, taken in real time, was discussed in a previous paper[39] for the case of plane-channel flow, and can be

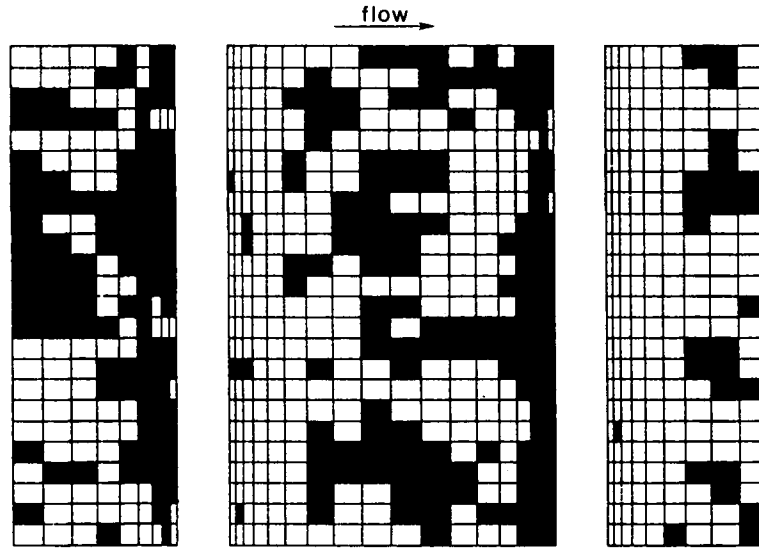


Figure 19. Ribbed channel ($Re^0 = 20\,000$): instantaneous temperature map on the ribbed wall (dark cells indicate $T_w < \bar{T}_w$, i.e. $Nu > \overline{Nu}$)

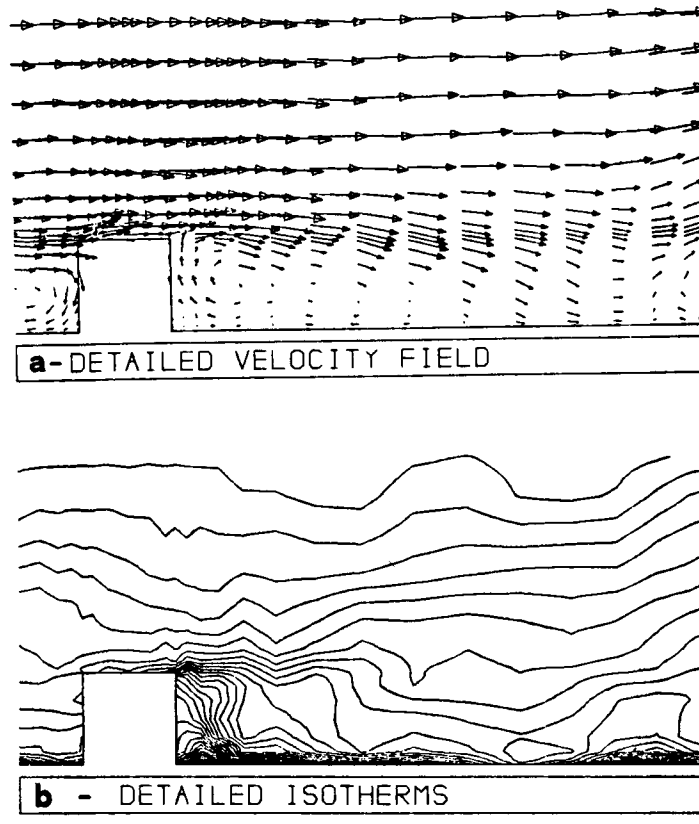


Figure 20. Ribbed channel ($Re^0 = 20\,000$): instantaneous temperature and velocity fields near a rib on a plane normal to $z$

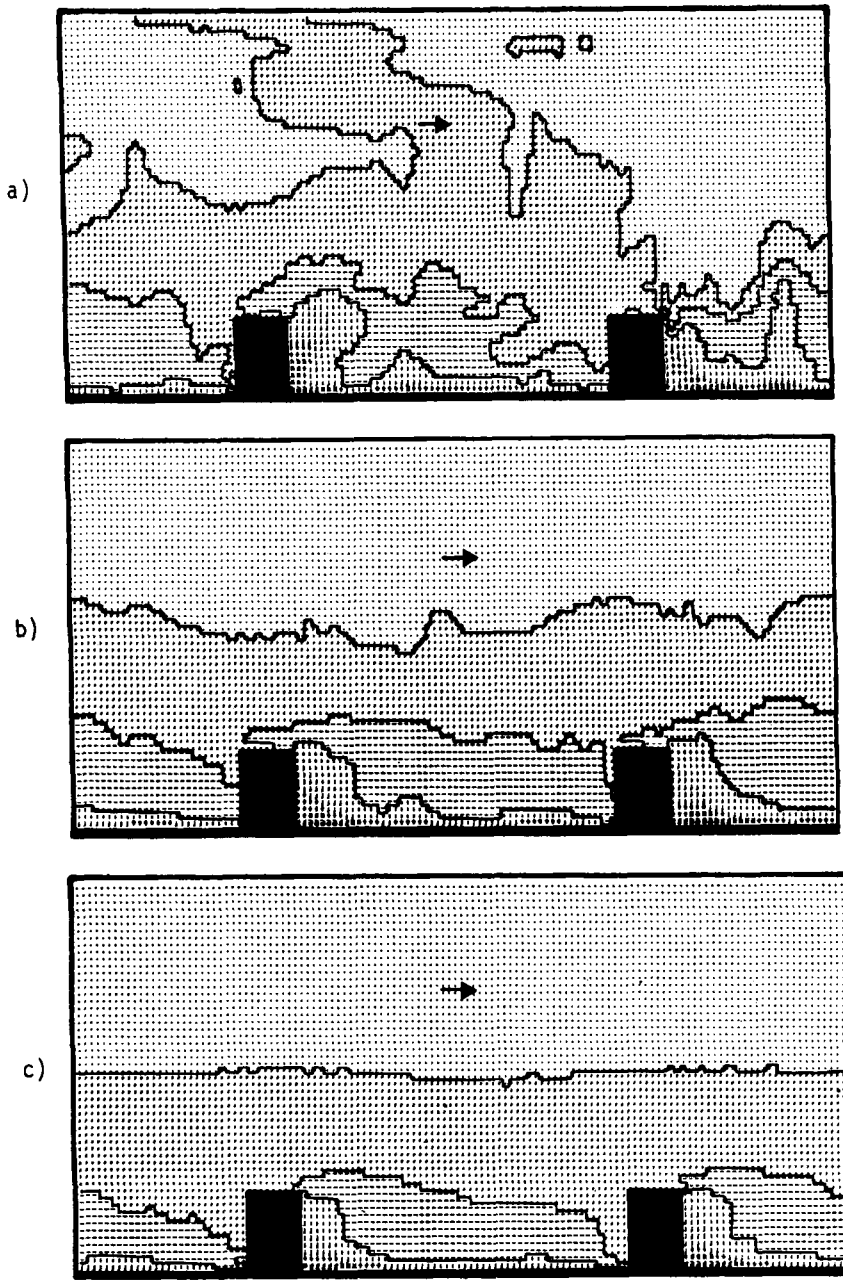


Figure 21. Ribbed channel ($Re^0 = 20\,000$): temperature distribution (the interval between consecutive isotherms is about 3·5 wall units). (a) $z = W/2$, $y = 40$ LETOTs (b) span-averaged, $t = 40$ LETOTs (c) $z = W/2$, time-averaged over 30–40 LETOTs

introduced for this more complex case; LES methods are a promising approach to the solution of such problems. Finally, graph (c) (bottom) is averaged in time over 30–40 LETOTs. Smoothing effects are even more pronounced than in the span-averaged graph. The resulting time-averaged temperature field (or rather its span average) is what would be recorded by long-exposure

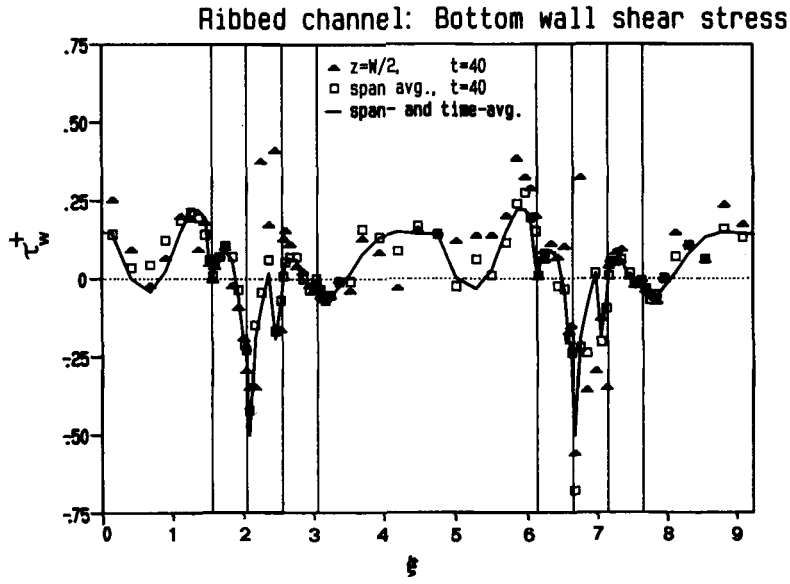


Figure 22. Ribbed channel ($Re^0 = 20\,000$): effect of span- and time averaging on the computed shear stress along the ribbed wall

interferograms or similar techniques. Note that at the present Reynolds number of 20 000, and for the flow of air in a wind tunnel $\sim 5$ cm in height, one LETOT corresponds to $\sim 5 \times 10^{-2}$ s, i.e. the averaging time of graph (c) would correspond to just 0·5 s of real time.

The effect of the various averages on *wall quantities* can be appreciated, for example, by considering Figure 22; here the whole simulated streamwise length of the channel, including two rib pitches, is represented. The abscissa is the distance $\xi$ travelled along the ribbed wall following the sides of the ribs; it is made dimensionless with respect to the rib height $h$. The quantities shown are $\tau_w$ (local instantaneous resolved streamwise wall shear stress), as computed at $z = W/2$ and $t = 40$ LETOTs; $\langle \tau_w \rangle$ (span-averaged instantaneous stress); and $\langle \bar{\tau}_w \rangle$ (span- and time-averaged stress, the time average being made over 10 LETOTs). The local and instantaneous profile exhibits strong space fluctuations; moreover, the profiles relative to the two rib pitches differ markedly from each other. Span averaging reduces the irregularities and makes the profiles over the two pitches closer to each other. Finally, span- and time averaging produces a smooth and periodic profile, repeating itself almost exactly over the two pitches. Similar remarks hold for the wall pressure and for the wall temperature or Nusselt number; see Reference 7.

Figures 23–25 report wall quantities ($p_w$, $\tau_w$ and $Nu$). LES results were averaged at each streamwise location over the channel span, and further averaged in time over 30–40 LETOTs. Moreover, the profiles relative to the two rib pitches included in the computational domain were averaged to improve the statistical quality of the results. The abscissa in Figures 23–25 is defined as in Figure 22.

Figure 23 reports streamwise profiles of the wall pressure, made dimensionless with respect to $\frac{1}{2}\rho\,(u_{max})^2$ (in which $u_{max}$ is the maximum velocity in the channel). The mean streamwise pressure gradient was subtracted from results, so that only the periodic component of the pressure is actually shown. The pressure was arbitrarily set to zero in the position midway between two consecutive ribs. $k$–$\varepsilon$ predictions obtained using Harwell-FLOW3D, and experimental data of

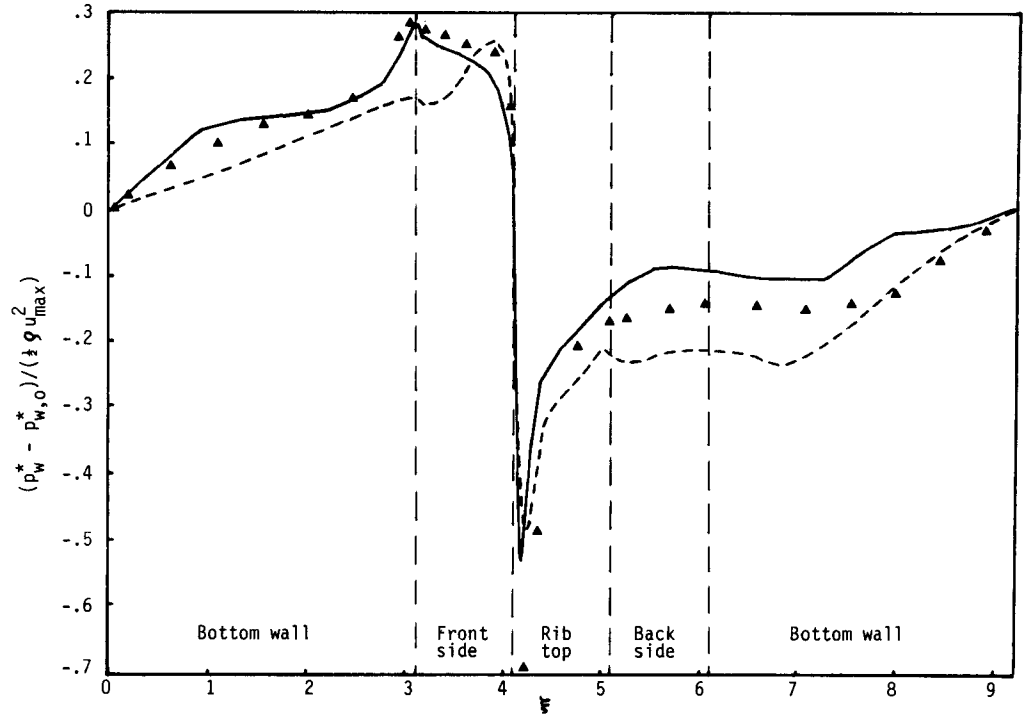


Figure 23. Ribbed channel: profiles of the static pressure along the ribbed wall. (———) Present predictions (LES, $h/H = 1/4{\cdot}8$, $Re^0 = 20\,000$); (– – –) $k$–$\varepsilon$ predictions ($h/H = 1/4{\cdot}8$, $Re = 20\,000$); (▲) Experiments (Kacker 1971, $h/H = 1/8$, $Re = 50\,000$

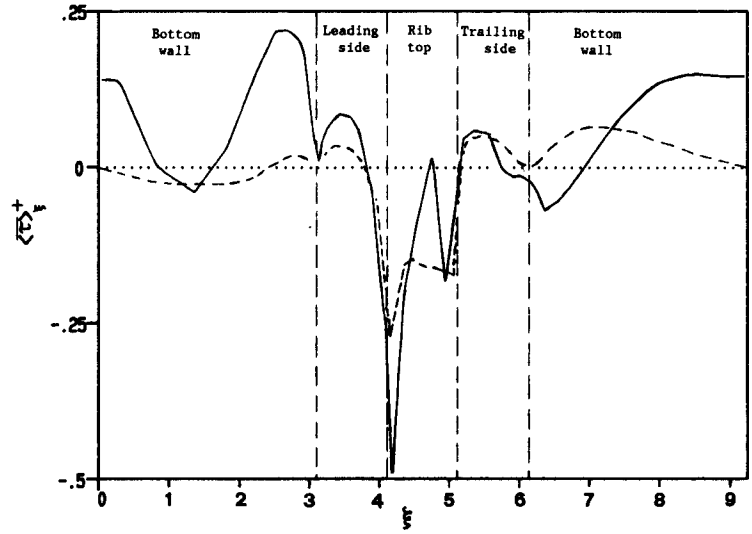


Figure 24. Ribbed channel: profiles of the shear stress in the direction along the ribbed wall. (———) Present predictions (LES, $h/H = 1/4{\cdot}8$, $Re^0 = 20\,000$) (– – –) $k$–$\varepsilon$ predictions ($h/H = 1/4{\cdot}8$, $Re = 20\,000$)

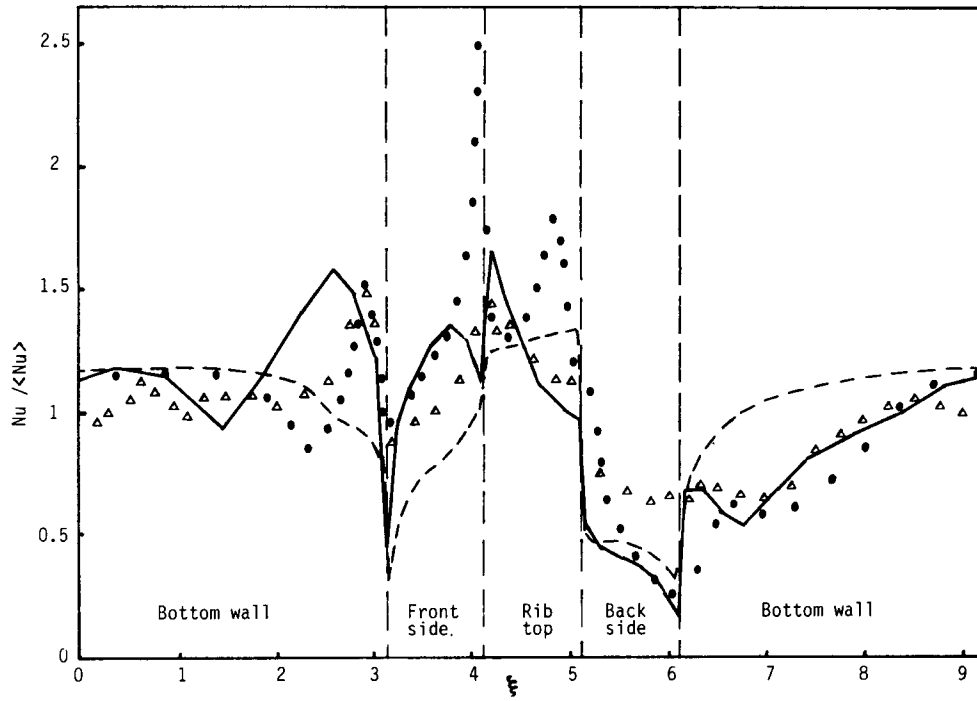


Figure 25. Ribbed channel: profiles of the Nusselt number along the ribbed wall. (———) Present predictions (LES, $h/H=1/4{\cdot}8$, $Re^0=20\,000$); (– – –) $k$–$\varepsilon$ predictions ($h/H=1/4{\cdot}8$, $Re=20\,000$); (●) Experiments (Lockett[33] $h/H=1/9{\cdot}5$, $Re=30\,000$); (△) Experiments (Watts and Williams[52] $h/H=1/8$, $Re=82\,000$)

Kacker[42] obtained for $Re=50\,000$ in a channel having $H/h=8$, are also reported in a similar form for comparison. Taking into account the above remarks on comparisons with different geometries and Reynolds numbers, the qualitative agreement with experimental data is encouraging, generally comparable with that obtained by the $k$–$\varepsilon$ model, and much better in the region of the leading side of the rib.

Figure 24 shows similar profiles of the wall shear stress in the streamwise direction, $\tau_w$. $k$–$\varepsilon$ results are also reported for comparison. No accurate experimental data seem to have been reported in the literature for this quantity. Values are normalized to $\tau$, i.e. the mean, or nominal, wall shear stress, defined by equation (12). Values of $\tau_w$ differ broadly from $k$–$\varepsilon$ predictions; the LES wall shear stress profile indicates that reattachment occurs about four rib heights downstream of each rib, and is followed by a short direct flow region and then by reseparation $\sim 1{\cdot}5$ rib heights upstream of the consecutive rib. A counter-rotating corner eddy is also clearly indicated by negative values of $\tau_w$ downstream of a rib. These results, especially as regards the reattachment length, are in agreement with experimental findings for comparable pitch-to-height and blockage ratios. Drain and Martin[50] reported a reattachment length of $4{\cdot}3\,h$ for $P_1/h=7{\cdot}2$, $h/H=1/5$ (practically coincident with the values used in the simulation). $k$–$\varepsilon$ computations underpredict severely this important parameter, giving about $3h$ in the present case.

Figure 25 shows span- and time-averaged profiles of the Nusselt number, defined by equation (18). Here, we concentrate on the *qualitative* behaviour of $Nu$ along the ribbed wall; thus, profiles

Table I. Comparison of mean Nusselt number (scaled)

| | LES | $k$–$\varepsilon$ | Watts and Williams[52] | Lockett[33] |
|---|---|---|---|---|
| $h/H$ | 1/4·8 | 1/4·8 | 1/8 | 1/9·5 |
| $Re$ | 26 600 | 21 000 | 82 000 | 30 000 |
| $Nu$ (scaled) | 154 | 150 | 140 | 142 |

are normalized to the corresponding averaged value, $Nu$, to facilitate comparison with

(a) $k$–$\varepsilon$ results, obtained with Harwell-FLOW3D for the same pressure drop and channel geometry;
(b) experimental results of Watts and Williams,[52] obtained by the copper-foil technique in a channel having $h/H = 1/8$ at $Re = 82\,000$;
(c) experimental results of Lockett,[33] obtained by holographic interferometry in the City University wind tunnel (having $h/H = 1/9{\cdot}5$) at $Re = 30\,000$.

LES predictions present many features that agree with experimental data, and differ from $k$–$\varepsilon$ results. The overall streamwise profile of $Nu$, with an absolute sharp maximum shortly upstream of each rib and a secondary flat maximum at $\sim 2/3$ of the distance between ribs (i.e. in the reattachment region) is correctly reproduced. Note also the relative minimum shortly downstream of the rib, probably in correspondence with backflow separation (edge of a counter-rotating eddy). This graph should be compared with the instantaneous temperature map in Figure 19. These features are totally missing in the $k$–$\varepsilon$ predicted profile, which appears practically flat over the whole interrib gap.

As experimental data were obtained for different ratios of rib height to duct height ($h/H$) and for different Reynolds numbers, the levels and the average values of the Nusselt number cannot be compared directly with LES predictions on a quantitative basis. However, some comparison can be drawn if values of $Nu$ are scaled to the present $h/H$ (1/4·8) and $Re$ (26 600) by using Rapier's correlation (19). $k$–$\varepsilon$ results for $Nu$ can be scaled by using the same law; note that $k$–$\varepsilon$ simulations (for the same pressure drop as in LES) gave a Reynolds number of $\sim 21\,000$, in good agreement with correlations (15)–(17). Results are summarized in Table I. It shows that, within the limits of validity of equation (19), LES predicts a value of $Nu$ comparable with both $k$–$\varepsilon$ and experimental results. Cross-stream profiles of mean velocity and temperature, and of fluctuating velocity components, are reported in Figures 26 and 27 for the two streamwise positions A and B indicated in Figure 2(b); they are in dimensionless form, equation (14), and are compared with $k$–$\varepsilon$ predictions using Harwell-FLOW3D for the same pressure drop.

On profiles of $\langle u \rangle$, Figure 26, the most relevant disagreement is in the consistently higher value of bulk velocity, and in the backflow region predicted by LES, but not by the $k$–$\varepsilon$ model, midway between ribs (section A). Profiles of $\langle T \rangle$ agree fairly well on section B but LES predictions are lower (i.e. heat transfer rates are higher) at section A. Levels of $k$, Figure 27, agree on the whole with $k$–$\varepsilon$ predictions; the most relevant difference is in the sharp peak predicted by LES just over the rib top, Figure 27(b), and mainly associated with a peak in $u''_{\mathrm{rms}}$.

Cross-stream profiles of the mean streamwise velocity and of the streamwise fluctuation, computed by LES for $h/H = 1/4{\cdot}8$ and $Re^0 = 40\,000$, are reported in Figure 28 for the two streamwise locations A and B. They are compared with experimental results of Bates *et al.*[48] and of Drain and Martin,[50] obtained for $h/H = 1/5$ and Reynolds numbers of 50 000 and 64 000,

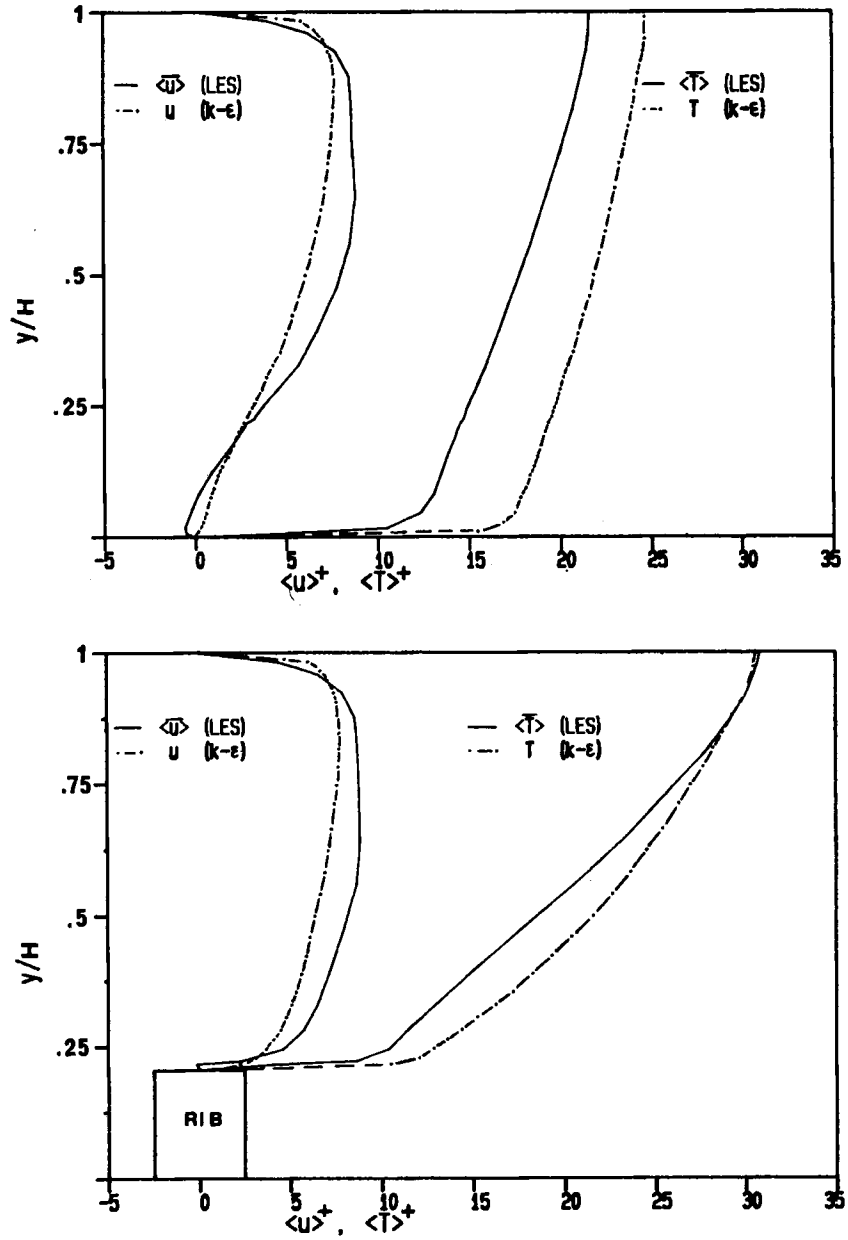


Figure 26. Ribbed channel: cross-stream profiles of mean $u$ and $T$ at the two sections A and B, see Figure 2(b)

respectively. For the mean velocity, also $k$–$\varepsilon$ predictions using the TUFC code are reported from Reference 50. Profiles are normalized to the mean velocity $u_B$ over the rib top, or to its square.

Experimental profiles of the mean velocity confirm that the main recirculation region extends beyond one-half the distance between consecutive ribs. This is correctly predicted by LES, while $k$–$\varepsilon$ results show no backflow at section A. The experimental streamwise fluctuation profiles at

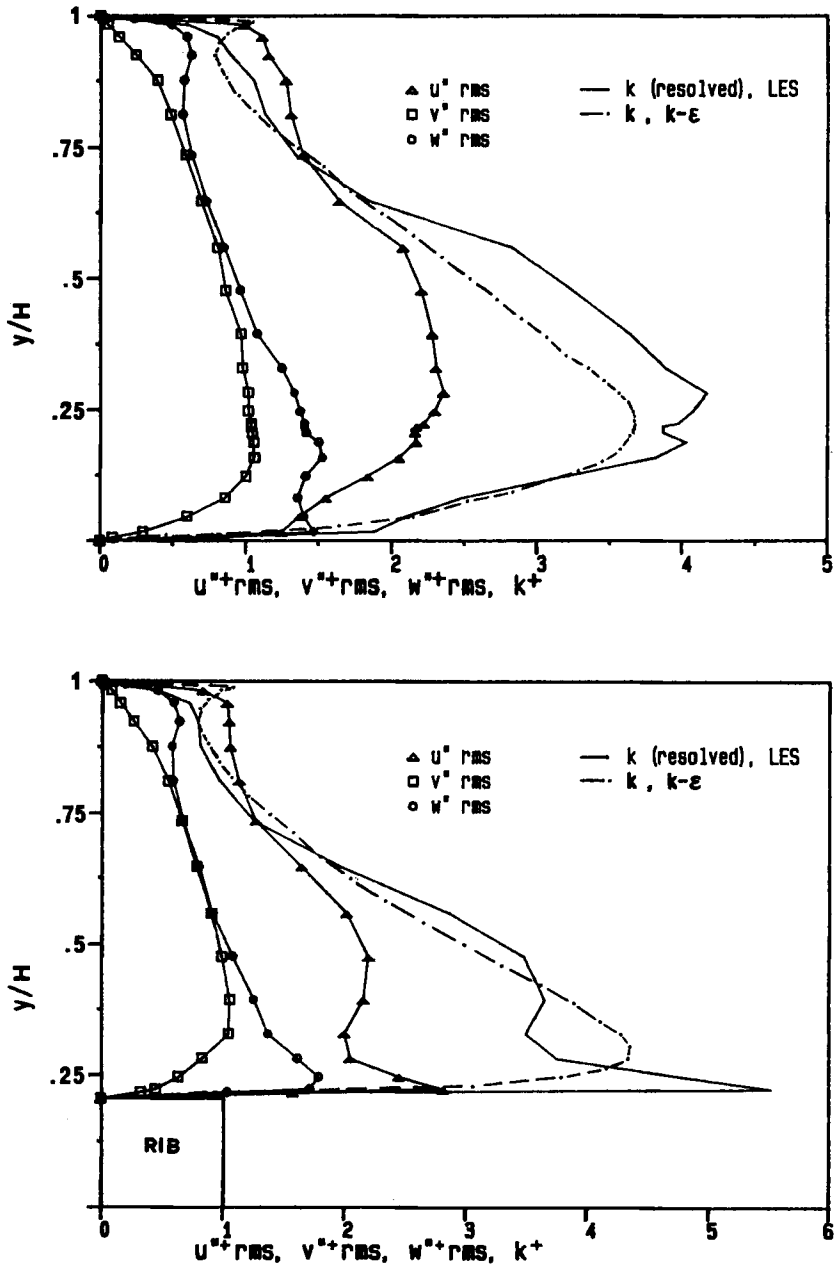


Figure 27. Ribbed channel: cross-stream profiles of fluctuations at the two sections A and B, see Figure 2(b)

section B exhibit a sharp peak just above the rib top, which is correctly predicted by LES but not by the $k$–$\varepsilon$ model. On both sections A and B, LES overpredicts slightly the turbulence levels in the bulk flow region. The disagreement between the two sets of experimental data as regards the fluctuation intensity near the smooth wall should also be noticed.

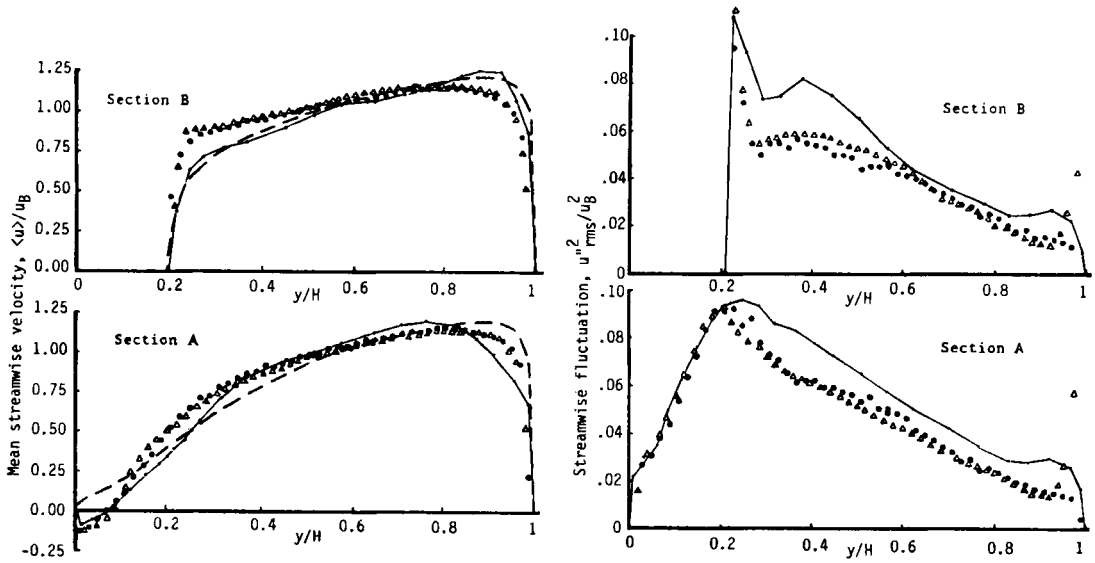


Figure 28. Ribbed channel: comparison of computed and experimental cross-stream profiles of mean and fluctuating streamwise velocity (values are normalized with respect to the average velocity over a rib, $u_B$). (· ——— ·) Present predictions (LES $h/H = 1/4{\cdot}8$, $Re^0 = 40\,000$); (– – –) $k$–$\varepsilon$ predictions using the TUFC code;[50] (●) Experiments (Drain and Martin,[50] $h/H = 1/5$, $Re = 64\,000$); (△) Experiments (Bates *et al.*,[48] $h/H = 1/5$, $Re = 50\,000$)

## 5. CONCLUSIONS

The main purpose of the present work was to demonstrate the feasibility of LES flow and heat transfer predictions for both simple and complex (recirculating) flows using a general-purpose code, a simple subgrid model and relatively coarse grids. This purpose was essentially reached; 40 LETOT simulations required about 90 m for the plane channel flow (with 22 984 grid points) and 130 m for the ribbed duct (33 800 points) on a CRAY-2 computer. Analysis of the behaviour of $k^+$ for this latter (Figure 3) shows that shorter simulations (10 LETOTs, requiring 30 m of CPU time) may be sufficient to get independence from initial conditions and acceptable statistics.

For the simpler flow (smooth channel) several high-quality LES predictions are known. The present simulations suffer mainly from insufficient resolution of the computational domain, which results in overprediction of the average velocity, of the temperature drop, and of the streak spacing near the walls. Turbulence quantities, however, are predicted satisfactorily and coherent near-wall structures are qualitatively reproduced.

For the more complex flow (periodic ribs) this study is one of the first presented so far. Statistically stationary conditions are reached after a few LETOTs. The mean flow rate is overpredicted as compared with experimental correlations and $k$–$\varepsilon$ simulations, and so are turbulence levels in the bulk flow region. However, the overall flow structure and many fine features of the mean and fluctuating flow field are in good qualitative agreement with existing experimental data. Certain flow features are correctly predicted by LES but absent from $k$–$\varepsilon$, notably involving recirculation. It should be stressed that this is achieved by using a very simple model, containing only a few 'adjustable' constants ($c_s$, $A^+$ and, for heat transfer predictions, $\sigma_s$).

However, the main point at issue is not whether LES performs better than the $k$–$\varepsilon$ or similar closure models. The amount of information provided by a three-dimensional, time-dependent

simulation of a turbulent flow is incomparably larger than that given by any time-average-based turbulence model; under some circumstances, this may overcome the disadvantage of a less accurate prediction of some mean property of the flow, especially as far as the simulation is used as a tool to help understand the physical mechanisms involved.

It is perhaps surprising that the overall quality of the predictions, for example, regarding the establishment of statistical equilibrium, is better for the more complex flow than for the simpler one. However, it should be observed that a turbulent flow within simple boundaries may be quite complex in its internal structure, while in a geometrically complex domain the flow characteristics are more heavily conditioned by the geometry* and may be relatively easier to predict (a well-known analogue in external flows is separation over sharp corners versus separation from a smooth surface). Moreover, for basic geometries such as a plane channel a large amount of experimental information is available and has been used throughout the years to 'tune' existing turbulence models. For more complex geometries, especially involving separation and reattachment, most existing models present *some* drawback and LES can be more competitive.

Future work with LES will involve the investigation of alternative wall boundary conditions for high-Reynolds-number simulations; the testing of alternative differencing schemes; and the extension of the simulations to other geometries such as backward-facing steps and cross-corrugated heat transfer elements.

The work reported here is part of a parallel research programme at City University involving both conventional turbulence modelling and LES, and corresponding experimental work. The latter includes holographic interferometry for heat transfer measurements, and was reported in some detail, for example, in Reference 71. The new method of holocinematographic velocimetry[72] has both three-dimensional and transient capabilities, and it is intended to commence work with this also. Finally, both with LES and experiment there is the consequence of entering the currently important field of coherent structure research.[73]

ACKNOWLEDGEMENTS

Computational facilities for the present simulations were partly provided by the Computer Science and Systems Division at the A.E.R.E. Harwell. Support from the U.K. Science and Engineering Research Council/A.E.R.E. Harwell Cooperative Research Grant GR/C 90577 is gratefully acknowledged. One of the authors (M. Ciofalo) was supported by a NATO grant (I.R.T. Award No. 0769/86). The authors thank Dr. Ian P. Jones and the development team of the Harwell-FLOW3D code for their help and interest.

## APPENDIX: NOMENCLATURE

| | |
|---|---|
| $A^+$ | constant in the near-wall damping law |
| $c_s$ | constants in the Smagorinsky subgrid model |
| $C_f$ | friction coefficient |
| $C_p$ | specific heat at constant pressure |
| $D$ | near-wall damping factor |
| $D_e$ | hydraulic diameter |

* Experimental evidence from our holographic interferometry work[33] tends to support this; the fringes were rather sharper with the roughness element geometry than the smooth wall, indicating that the former may partially 'suppress' the spanwise structures of the smooth wall.

| | |
|---|---|
| $H$ | channel height |
| $h$ | rib height |
| $k$ | turbulent kinetic energy |
| $L$ | length of the computational domain |
| LETOT | Large Eddy Turn Over Time, $\delta/u_\tau$ |
| $\dot{M}$ | mass flow through the channel |
| $Nu$ | Nusselt number, $qD_e/[\lambda(T_w-\hat{T})]$ |
| $p$ | static pressure |
| $P$ | modified pressure, $p+(2/3)\rho k$ |
| $P^*$ | periodic component of $P$ |
| $P_i$ | rib pitch |
| $q$ | heat flux per unit surface |
| $Re$ | Reynolds number, $\hat{u}D_e/\nu$ (based on hydraulic diameter) |
| $Re_\delta$ | Reynolds number, $\hat{u}\delta/\nu$ (based on channel half-height) |
| $S_u$ | source term in the streamwise momentum equation |
| $S_T$ | source term in the temperature equation |
| $S_{ij}$ | strain rate tensor, $\frac{1}{2}(\partial u_i/\partial x_j+\partial u_j/\partial x_i)$ |
| $t$ | time |
| $T$ | temperature |
| $T^*$ | periodic component of $T$ |
| $u, v, w$ | velocity components along $x, y, z$ |
| $u_\tau$ | friction velocity, $(\lvert\tau\rvert/\rho)^{1/2}$ |
| $W$ | width of the computational domain |
| $x, y, z$ | co-ordinates |
| $x_R$ | reattachment length |

*Greek letters*

| | |
|---|---|
| $\alpha$ | thermal diffusivity, $\lambda/(\rho C_p)$ |
| $\alpha_s$ | subgrid thermal diffusivity |
| $\delta$ | channel half-height, $H/2$ |
| $\Delta$ | average size of a computational cell |
| $\Delta x, \Delta y, \Delta z$ | dimensions of control volumes along $x, y, z$ |
| $\Delta t$ | time step |
| $\varepsilon$ | dissipation of turbulent kinetic energy |
| $\lambda$ | thermal conductivity |
| $\nu$ | kinematic viscosity |
| $\nu_s$ | subgrid kinematic viscosity |
| $\xi$ | non-dimensional distance along ribbed wall |
| $\rho$ | density |
| $\sigma$ | Prandtl number, $C_p\rho\nu/\lambda$ |
| $\sigma_s$ | subgrid Prandtl number |
| $\tau_w$ | local wall shear stress |
| $\tau$ | mean wall shear stress, $\delta\, \mathrm{d}\hat{p}/\mathrm{d}x$ |

*Superscripts and averages/fluctuations*

| | |
|---|---|
| $Q$ | generic scalar (resolved component) |
| $Q^+$ | dimensionless value |

| | |
|---|---|
| $Q^0$ | initial/nominal value |
| $\bar{Q}$ | time average |
| $\langle Q \rangle$ | space average over a plane or a span |
| $Q$ | space average over the channel cross-section |
| $Q''$ | space fluctuation $Q - \langle Q \rangle$ |
| $Q''_{\text{rms}}$ | root mean square value of $Q''$, $\langle Q''^2 \rangle^{1/2}$ |

## REFERENCES


1. D. B. Spalding, 'Discussion on "Turbulence Models for Heat Transfer", *Proc. 6th Int. Heat Transfer Conf.*, Toronto, Canada, 1978, vol. 8 (Discussions), p. 8, Hemisphere, Washington.
2. P. R. Voke and M. W. Collins, 'Large Eddy Simulation: Retrospect and Prospect', *Physico Chem. Hydrodyn.*, **4**, 119–161 (1983).
3. A. D. Burns, I. P. Jones, J. R. Kightley and N. S. Wilkes, 'Harwell-FLOW3D, release 2.1—user manual', *Harwell Report AERE-R* (Draft), August 1988.
4. J. H. Fergizer, 'Large eddy numerical simulations of turbulent flows', *AIAA J.*, **15**, 1261–1267 (1977).
5. G. Grötzbach, 'Direct numerical and large eddy simulation of turbulent channel flows', in N.P. Cheremisinoff (ed.), Encyclopaedia of Fluid Mechanics, vol. 6, Gulf. Publishing Co., 1986.
6. M. Ciofalo, 'Computation of turbulent recirculating flows with heat transfer using FLOW3D', progress report, January–April 1988 (large-eddy simulation), *TFERC Res. Memo. No. TF 89/01/01*, The City University, London, 1989.
7. M. Ciofalo, 'Computation of turbulent recirculating flows with heat transfer using FLOW3D', Progress report, September–October, 1988 (large-eddy simulation II), *TFERC Res. Memo. No. TF/01.06.89*, The City University, London, 1989.
8. J. Smagorinsky, General circulation with the primitive equations: part I. The basic experiment, *Mon. Weather Rev.*, **91**, 99–164 (1963).
9. E. R. Van Driest, 'On turbulent flow near a wall', *J. Aero. Sci.*, **23**, 1007–1011 (1956).
10. P. J. Mason and N. S. Callen, 'On the magnitude of the subgrid-scale eddy coefficient in large-eddy simulations of turbulent channel flow', *J. Fluid Mech.*, **162**, 439–462 (1986).
11. J. C. Hunter, H. M. Tsai, J. F. Lockett, P. R. Voke, M. W. Collins and D. C. Leslie, 'A Comparison of Large Eddy Simulation Predictions of a Thermal Layer with Holographic Interferometry', *Proc. 5th Int. Conf. Num. Methods for Thermal Problems*, Montreal, 1988.
12. M. Antonopoulos-Domis, 'Large eddy simulation of a passive scalar in isotropic turbulence', *J. Fluid Mech.*, **104**, 55–79 (1981).
13. T. Kobayashi, M. Kano and T. Ishihara, 'Prediction of turbulent flow in two-dimensional channel with turbulence promoters'. (a) 1st Report, 'Numerical predictions by large eddy simulation', *Bull. JSME*, **27**, 1893–1898 (1984). (b) 2nd Report, Numerical prediction by $k$–$\varepsilon$ Model and comparison with experimental results (with Saga, T.), *Bull. JSME*, **28**, 2940–2947 (1985). (c) 3rd Report, Improvement of large eddy simulation and formation of streaklines, *Bull. JSME*, **28**, 2948–2953 (1985).
14. J. W. Deardorff, 'Three-dimensional numerical modeling of the planetary boundary layer', in D. A. Haugen (ed.), Workshop on Micrometeorology, Chapter 7, Am. Met. Soc., Boston, 1973 pp. 271–309.
15. G. Comte-Bellot, Contribution a l'Etude de la turbulence de conduite, Doctoral Thesis, Univ. of Grenoble, France, 1963.
16. U. Piomelli, J. H. Ferziger, P. Moin and J. Kim, 'New approximate boundary conditions for large-eddy simulations of wall-bounded flows', *Phys. Fluids* A, **1**, 1061–1068, (1989).
17. G. S. Beavers and E. M. Sparrow, 'Low Reynolds number flow in large aspect ratio ducts', *ASME J. of Basic Eng.*, **38**, 181 (1971).
18. A. C. Rapier, 'A correlation of flow and heat transfer data for surfaces roughened with transverse square ribs of pitch-to-height ratio of 7.2', *UKAEA Report ND/R/63(W)*, 1977.
19. M. Ciofalo, 'Algorithms and Auxiliary Routines for FLOW3D, Release 2', *TFERC Res. Memo. No. TF/03/88/01*, The City University, London, 1988.
20. C. M. Rhie and W. L. Chow, 'Numerical study of the turbulent flow past an airfoil with trailing edge separation', *AIAA J.*, **21**, 1527–1532 (1983).
21. A. D. Burns, and N. S. Wilkes, 'A finite-difference method for the computation of fluid flows in complex three-dimensional geometries', *Harwell Report AERE-R 12342*, July 1987; see also updated version, October 1989.
22. S. Gavrilakis, Personal communication, 1988.
23. M. Ciofalo, 'Computation of turbulent recirculating flows with heat transfer using FLOW3D', *Progress report, October–December 1987, TFERC Res. Memo. No. TF. 02/88/01*, The City University, London, 1988.
24. M. Ciofalo and M. W. Collins, 'Time-dependent numerical simulation of the starting flow of an incompressible fluid past a backward-facing step', Paper No. 37, *Proc. AGARD Symposium Validation of Computational Fluid Dynamics*, Lisbon, Portugal, 2–5 May, 1988.

25. R. I. Issa, 'Solution of the implicitly discretized fluid flow equations by operator-splitting', *J. Comp. Phys.*, **62**, 40–65 (1986).
26. S. V. Patankar and D. B. Spalding, 'A calculation procedure for heat, mass and momentum transfer in three-dimensional parabolic flows', *Int. J. Heat Mass Transfer*, **15**, 1787–1806 (1972).
27. J. P. VanDoormal and G. D. Raithby, 'Enhancements of the SIMPLE method for predicting incompressible fluid flows', *Numer. Heat Transfer*, **7**, 147–163 (1984).
28. H. L. Stone, 'Iterative solution of implicit approximations of multidimensional partial differential equations', *SIAM J. Numer. Anal.*, **5**, 530–558 (1968).
29. J. R. Kightley, 'The conjugate gradient method applied to turbulent flow calculations', *Harwell Report AERE CSS 184, HL85/1584*, October 1985 (*6th GAMM Conf. on Numerical Methods in Fluid Mechanics*, Gottingen, September 1985).
30. J. Laufer, 'The structure of turbulence in fully developed pipe flow', *NACA Report No. 1174*, 1954.
31. H. P. Kreplin and H. Eckelmann, 'Behavior of three fluctuating velocity components in the wall region of a turbulent channel flow', *Phys. Fluids*, **22**, 1233–1239 (1979).
32. A. K. M. F. Hussain and W. C. Reynolds, 'Measurements in fully developed turbulent channel flow', *ASME J. Fluids Eng.* **97**, 568–580 (1975).
33. J. F. Lockett, 'Heat transfer from roughened surfaces using laser interferometry', *Ph.D. Thesis*, Department of Mechanical Engineering, The City University, London, 1987.
34. J. W. Deardorff, 'A numerical study of three-dimensional turbulent channel flow at large Reynolds numbers', *J. Fluid Mech.*, **41**, 453–480 (1970).
35. P. Moin and J. Kim, 'Numerical investigation of turbulent channel flow', *J. Fluid Mech.*, **118**, 341–377 (1982).
36. U. Schumann, 'Subgrid scale model for finite difference simulations of turbulent flows in plane channels and annuli', *J. Comp. Phys.*, **18**, 376–404 (1975).
37. K. Horiuti, 'Large eddy simulation of turbulent channel flows', *Proc. EUROMECH 199, 'Direct and Large Eddy Simulation of Turbulent Flows'*, Technical University of Munich, W. Germany, 30 September–2 October, 1985.
38. K. A. Azab and J. B. McLaughlin, 'Modeling the viscous wall region', *Phys. Fluids*, **30**, 2362–2373 (1987).
39. M. Ciofalo, T. R. Fodemski and M. W. Collins, 'Large eddy simulation of turbulent flow and heat transfer in plane channels', *Proc. 6th Nat. Conf. of the UIT (Unione Italiana di Termofluidodinamica)*, Bari, Italy, 9–11 June 1988.
40. W. Nakayama, 'Enhancement of heat transfer', *Proc. 7th Int. Heat Transfer Conf.*, Munich, 1982, vol. 1, pp. 223–240.
41. P. L. Mantle, A new type of roughened heat transfer surface selected by flow visualisation techniques', *Proc. 3rd Int. Heat Transfer Conf.*, Chicago, 1966, vol. 1, pp. 45–55.
42. S. C. Kacker, 'Estimation of friction factor of rough surfaces from the pressure distribution around a roughness element', *CEGB Report RD/B/N 1967*, 1971.
43. F. Durst and A. K. Rastogi, 'Theoretical and Experimental investigations of turbulent flows with separation', in I. F. Durst *et al.* (eds), *Procs. 1st Symp. Turb. Shear Flows*, Pennsylvania State University, University Park, PA, 18–20 April 1977, Springer, Berlin, 1979.
44. F. Durst and A. K. Rastogi, Turbulent flow over two-dimensional fences, in L. J. S. Bradbury *et al.* (eds), *Proc. 2nd Symp. Turb. Shear Flows, Imperial College, London*, 1979, Springer, Berlin, 1980.
45. K. Hanjalic and B. E. Launder, 'Fully developed asymmetric flow in a plane channel', *J. Fluid Mech.*, **51**, 301 (1972).
46. J. A. C. Humphrey and J. H. Whitelaw, 'Turbulent flow in a duct with roughness', in L. J. S. Bradbury *et al.* (eds), *Proc. 2nd Symp. Turb. Shear Flows*, Imperial College, London, 1979, Springer, Berlin, 1980.
47. C. J. Lawn, 'Flow measurements to establish the mechanism of heat transfer from a rib roughened surface', *CEGB Report RD/B/N 3514*, 1976.
48. C. J. Bates, M. L. Yeoman and N. S. Wilkes, 'Non-intrusive measurements and numerical comparison of the axial velocity components in a two-dimensional flow channel for a backward-facing step and a rib-roughened surface', *Harwell Report AERE-R 10787*, 1983.
49. S. J. Cocking and W. Dalzell, 'Two component velocity measurements on turbulent flow in a ribbed-wall flow channel and comparison with a turbulent energy—dissipation model', *UKAEA Report AERE-R 11231*, 1984.
50. L. E. Drain and S. Martin, 'Two component velocity measurements of turbulent flow in a ribbed-wall flow channel', *Proc. Int. Conf. on Laser Velocimetry—advances and Applications*, Manchester, U.K. 16–18 December, 1985.
51. D. Wilkie, 'Forced convection heat transfer for surfaces roughened by transverse ribs', *Proc. 3rd Int. Heat Transfer Conf.*, Chicago, 1966, Vol. 1, pp. 1–9.
52. J. Watts and F. Williams, 'A technique for the measurement of local heat transfer rates using copper foil', *CEGB Report RD/B/5023 N81, HTSG/N(81)18*, April 1981.
53. J. F. Lockett, J. C. Hunter, P. R. Voke and M. W. Collins, 'Investigation of convective heat transfer enhancement using real-time holographic interferometry', *Proc. 6th Int. Conf. on Photon Correlation and Other Optical Techniques in Fluid Mechanics*, University of Cambridge, U.K., July 1985.
54. P. L. Mantle, A. R. Freeman and J. Watts, 'Conductivity effects of ribbed surface heat transfer', *Int. J. Heat Mass Transfer*, **14**, 1825–1834 (1971).
55. J. A. C. Humphrey, 'Turbulent flow in an asymmetrically roughened duct of square cross section', in H. D. Thompson and W. H. Stevenson (eds), *Laser Velocimetry and Particle Sizing*, Hemisphere, 1979, p. 220.
56. N. S. Wilkes, 'Prediction of the turbulent fluid flow through a channel with rib roughened surfaces', *Harwell Report AERE-R 9874*, 1980.

57. N. S. Wilkes and R. J. Firth, 'Prediction of fluid flow over a transverse ribbed surface using finite difference methods with a $k$–$\varepsilon$ turbulence model', *CEGB Report RD/B/5098 N81, HTSG/N(80)32*, September 1981.
58. N. S. Wilkes, 'The prediction of heat transfer from surfaces roughened by transverse ribs', *Harwell Report AERE-R 10293*, 1981.
59. T. R. Fodemski 'The simulation of flow and heat transfer in channels with ribbed surfaces', *Procs. 2nd Int. Symp. on Transport Phenomena in Turbulent Flows*, University of Tokyo, Tokyo, Japan, 25–29 October 1987, pp. 867–880.
60. T. R. Fodemski and M. W. Collins, 'Flow and heat transfer simulations for two- and three dimensional smooth and ribbed channels', *Proc. 2nd UK Nat. Heat Transfer Conf.*, Glasgow, U.K., 14–16 September 1988, Mechanical Engineering Publications, London, 1988, pp. 845–860.
61. T. R. Fodemski, 'The performance analysis of a ribbed channel based on computer simulation of flow and heat transfer', *Procs. 7th Nat. Conf. of the UIT (Unione Italiana di Termofluidodinamica)*, Florence, Italy, 15–17 June 1989, pp. 97–108.
62. T. R. Fodemski, P. R. Voke and M. W. Collins, 'Flow simulation in channels with distorted geometry using a spectral code with coordinate transformation', *Int. j. numer. methods fluids* **7**, 227–290, 1987.
63. C. L. V. Jayatilleke, 'The influence of Prandtl number and surface roughness on the resistance of the laminar sublayer to momentum and heat transfer', in U. Grigull and F. Hahne (eds), *Progr. Heat Mass Transfer, Vol. 1*, 1969, pp. 197–329.
64. S. J. Kline, W. C. Reynolds, F. A. Schraub and P. W. Rundstuder, 'The structure of turbulent boundary layers', *J. Fluid Mech.*, **30**, 741–773 1967.
65. C. P. Jackson and K. H. Winters, 'A guide to post-processing using the TGIN language', *Harwell Report AERE-R* (draft), March 1989.
66. M. Ciofalo and M. W. Collins, 'Large-eddy simulation of turbulent flow in plane and rib-roughened channels', in C. Taylor *et al.* (eds), *Proc. 6th Int. Conf. Num. Meth. Lam. Turb. Flow*, Swansea, U.K., 11–15 July 1989, Pineridge Press, Swansea, U.K., 1989, Part 2, pp. 1869–1882.
67. M. Ciofalo and M. W. Collins, 'Predictions of heat transfer for turbulent flow in plane and rib-roughened channels using large eddy simulation', *Proc. 7th Nat. Conf. of the UIT (Unione Italiana di Termofluidodinamica)*, Florence, Italy, 15–17 June 1989.
68. E. M. Sparrow and W. Q. Tao, 'Enhanced heat transfer in a flat rectangular duct with streamwise-periodic disturbances at one principal wall', *J. Heat Trans.*, **105**, 851–861 (1983).
69. J. C. Han, L. R. Glicksman and W. M. Rohsenow, 'An investigation of heat transfer and friction for rib-roughened surfaces', *Int. J. Heat Mass Trans.*, **21**, 1143–1156 (1978).
70. J. C. Han, 'Heat transfer and friction in channels with two opposite rib-roughened walls', *J. Heat Trans.*, **106**, 774–781, (1984).
71. J. F. Lockett, J. C. Hunter and M. W. Collins, 'Problems in using holographic interferometry to resolve the four-dimensional character of turbulence. Part I: theory and experiment; Part II: image and data processing', *Int. J. Opt. Sensors*, **1**, 211–234 (1986).
72. L. M. Weinstein, G. B. Beeler and A. M. Lindermann, 'High speed holocinematographic velocimetry for studying turbulent flow control physics', *AIAA Paper 85-0526, AIAA Shear Flow Control Conference*, Boulder, Colorado, 11–14 March 1985.
73. A. K. M. F. Hussain, 'Coherent structures—reality and myth', *Phys. Fluids*, **26**, 2816 (1983).